

reaction can provide much information regarding the spectroscopy of Pd¹⁰⁴, but because of limited resolution the data were primarily of interest as a reaction-mechanism study. Comparison of the experimental angular distributions and energy dependence with DWBA theory furnishes excellent evidence that direct triton pickup is the dominant process. A strong j dependence for $l=1$ transitions was observed in the

data and well reproduced by DWBA triton-cluster transfer calculations.

ACKNOWLEDGMENTS

The authors acknowledge with appreciation assistance in the time-consuming (p, α) runs at various times from Dr. G. Andersson-Lindstroem, Dr. R. Parkinson, Dr. Y. S. Park, and J. Orloff.

Precise Measurement of the Muonic X Rays in the Lead Isotopes*

H. L. ANDERSON

Enrico Fermi Institute, University of Chicago, Chicago, Illinois 60637

AND

C. K. HARGROVE, E. P. HINCKS,† J. D. McANDREW,‡ AND R. J. McKEE

National Research Council of Canada, Ottawa, Canada

AND

R. D. BARTON AND D. KESSLER

Carleton University, Ottawa, Canada

(Received 5 May 1969)

The size and shape of the nuclear charge distribution was determined for the Pb isotopes from precise measurements of their μ -atomic transition energies. Use of the $2p$ - $1s$ transitions was avoided in determining the nuclear parameters because of the perturbation caused by the presence of the muon in the $1s$ orbit. A simple two-parameter Fermi distribution was used in the analysis, but the rms radius determined thereby should be fairly model-independent. We find $\langle r^2 \rangle^{1/2} = 5.4839 \pm 0.0028$ fm for Pb²⁰⁶. This quantity increases by 0.0139 ± 0.0011 fm in going to Pb²⁰⁸. The calculated energy of the $1s$ level is found to be too high by 6.8 ± 2.3 keV, an effect which we have interpreted as being due to nuclear polarization, although the inadequacies in our treatment of the radiative corrections and of the effect of nuclear motion may account for a part of this difference. The measurement of the $4f$ - $3d$ and $5g$ - $4f$ transition energies provides a check of the vacuum-polarization correction, which is just at the limit of the higher-order contributions. The intensity ratios $I(2p_{3/2}-1s_{1/2})/I(2p_{1/2}-1s_{1/2})$ are found to be anomalously low for all three Pb isotopes and by as much as $(12 \pm 3)\%$ in the case of Pb²⁰⁸. In general, the intensities are reasonably well described by a cascade calculation, but the indication is that radiationless transitions do occur which can raise the Pb nucleus to an excited state. We detect *prompt* nuclear γ rays corresponding to this process. Some 15μ -capture γ rays with yields ≥ 0.01 per μ capture are reported for Pb²⁰⁶. One with a yield of 0.18 per μ capture is attributed to the $\frac{3}{2}^+ \rightarrow \frac{1}{2}^+$ g.s. transition in Tl²⁰⁶, following the emission of one neutron.

I. INTRODUCTION

IN this paper, we present the results of a careful study of the muonic x-ray lines of the Pb isotopes, with particular emphasis on Pb²⁰⁶. Our purpose was to perform a high-precision absolute measurement of the energies of the principal transitions of the Pb isotopes and use these energies to determine the parameters of their nuclear charge distribution. Since the same quantities are also determined by electron-scattering measurements, it is of interest to see to what extent such complementary methods give consistent results. When made with sufficient precision, such measurements provide a demanding test of our understanding of

hydrogenlike atoms, including the applicable radiative corrections and the effects of nuclear structure. We were interested in finding out how far the calculation of the energy levels could be relied on to give correct results.

The early measurements of muonic x-ray energies were limited by the resolution of NaI spectrometers. The development of the Li-drifted Ge detector by Tavendale¹ improved the resolution by an order of magnitude and made possible energy measurements correspondingly more precise. In our previous work^{2,3}

¹ G. T. Ewan and A. J. Tavendale, *Can. J. Phys.* **42**, 2286 (1964).

² H. L. Anderson, C. K. Hargrove, E. P. Hincks, and A. J. Tavendale, in *Proceedings of the Twelfth International Conference on High Energy Physics, Dubna, 1964* (Atomizdat, Moscow, 1966), Vol. 1, p. 936.

³ H. L. Anderson, R. J. McKee, C. K. Hargrove, and E. P. Hincks, *Phys. Rev. Letters* **16**, 434 (1966).

* Research supported by the U. S. National Science Foundation and the National Research Council of Canada.

† Also at Carleton University, Ottawa, Canada.

‡ Present address: Memorial University of Newfoundland, St. Johns, Newfoundland, Canada.

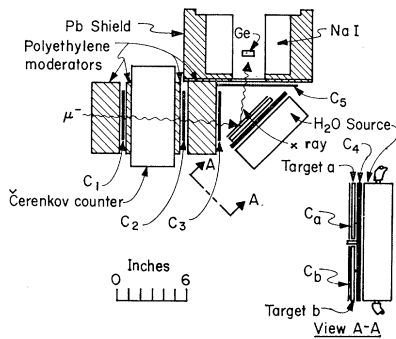


FIG. 1. Experimental layout.

with such detectors, the measurements were limited by instrumental effects other than detector resolution. In the present work, the apparatus was constructed to measure the muonic transition energies to an accuracy of 1 part in 10^4 .

This precision was achieved through improvements in analog-to-digital converters and through a calibration method which made use of the precisely known 511-keV differences between the double-escape, single-escape, and full-energy peaks observable in the Pb muonic x-ray spectrum. This was in addition to standard-reference γ rays which were recorded simultaneously with the x rays under the same beam-rate conditions. Digital stabilization was used to maintain the zero level and gain of the analog-to-digital converters, while linearity and stability were monitored continuously by a series of precision pulses. An on-line computer system facilitated the simultaneous collection of all these data.

The system was used to measure most of the principal spectral lines from Pb^{206} . The energies of the principal transitions up to $n=6$ were measured absolutely to 0.5 keV; the fine-structure splittings were measured to 0.2 keV. In addition, a number of weaker transitions were identified. The spectra of the three isotopes Pb^{206} , Pb^{207} , and Pb^{208} were intercompared, and the shifts in energy for the $2p-1s$ and $3d-2p$ transitions were determined.

The shape of the nuclear charge distribution in each of the Pb isotopes was determined by fitting the observed transition energies with those obtained by solving the Dirac equation for μ -atomic Pb. The nuclear charge was taken to be of the Fermi type and the two

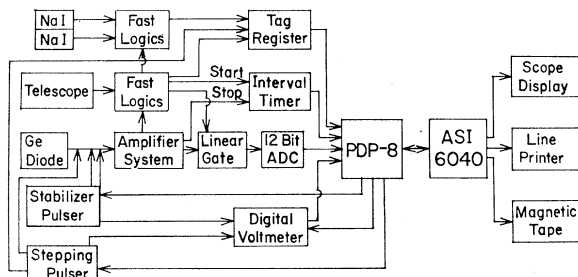


FIG. 2. Data flow and computer control system.

parameters of this distribution were varied until a best fit was obtained. Corrections due to vacuum polarization, Lamb shift, and the anomalous magnetic moment of the muon were included. An adequate fit could be obtained by depressing the calculated $1s$ energy by 6.8 ± 2.3 keV, an effect which we have tentatively interpreted as due to nuclear polarization by the muon.⁴

Section II describes the apparatus. Section III describes the data obtained for Pb^{206} . Section IV describes the peak fitting and the energy measurement. Section V describes the measurement of the isotope shift. Section VI describes the extraction of the nuclear-charge-distribution parameters. Section VII presents the measurements of the line intensities. Section VIII describes the nuclear γ -ray data. Section IX gives the conclusions.

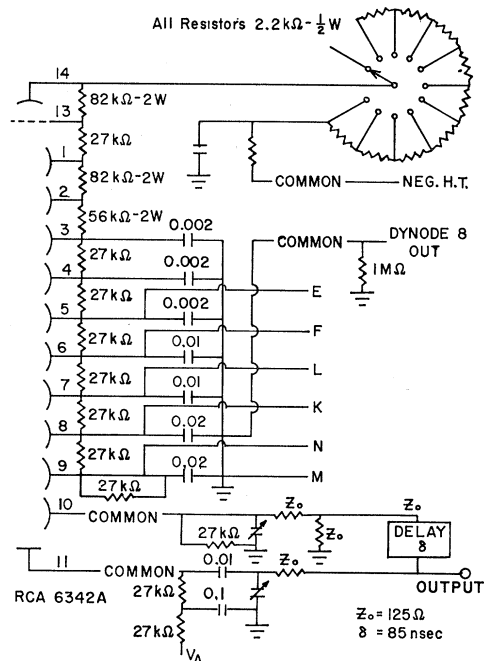


FIG. 3. Annulus photomultiplier circuit diagram.

II. APPARATUS

A. Muon Telescope

The forward muon beam of momentum 150 MeV/ c from the muon channel of the University of Chicago Synchrocyclotron was used. Measurements were made in two targets simultaneously,^{5,6} so that the relative displacements could be measured more accurately. They were arranged one above the other at 45° to the

⁴ H. L. Anderson, C. K. Hargrove, E. P. Hincks, J. D. McAndrew, R. J. McKee, and D. Kessler, *Phys. Rev. Letters* **22**, 221 (1969).

⁵ R. C. Cohen, S. Devons, A. D. Kanaris, and C. Nissim-Sabat, *Phys. Letters* **11**, 70 (1964).

⁶ R. D. Ehrlich, D. Fryberger, D. A. Jensen, C. Nissim-Sabat, R. J. Powers, B. A. Sherwood, and V. L. Telegdi, *Phys. Rev. Letters* **16**, 425 (1966); *Phys. Letters* **23**, 468 (1966).

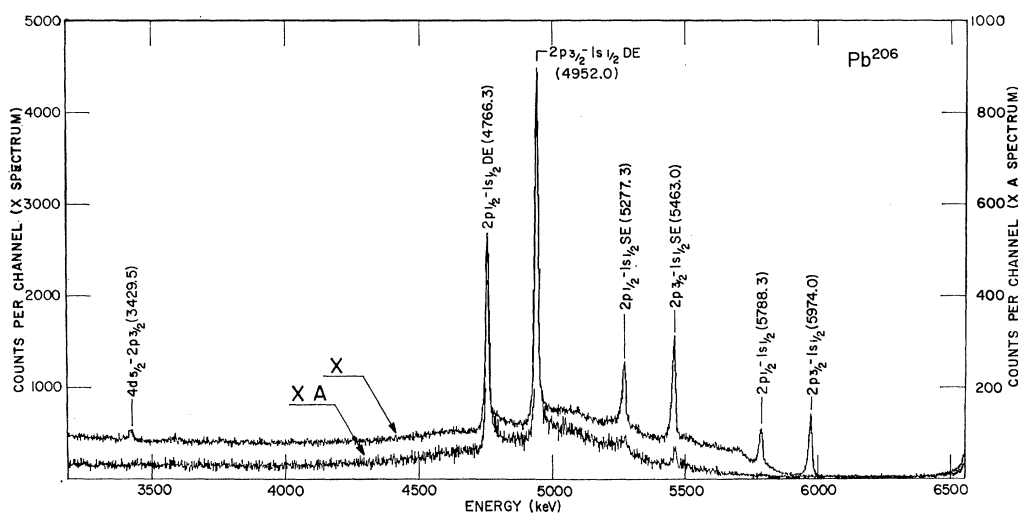


FIG. 4. High-energy end of prompt spectra in Pb^{206} . The X spectrum contains all prompt events, the XA spectrum the prompt events in coincidence with both halves of the NaI annulus.

beam. Typically, there were 1.5×10^4 μ stops per second in each target.

The arrangement is shown in Fig. 1. Counters C_1 , C_2 , and C_3 defined the muon beam. Counters C_a and C_b were flat against targets a and b and thus labeled stops in each target with high efficiency. Counter C_4 was operated in anticoincidence and vetoed events due to particles passing through the target. A ledge of scintillator was placed on counter C_4 between the targets to veto particles passing from one target into the other. Counter C_5 vetoed charged particles which could enter the Ge diode. The Čerenkov counter using FC75 liquid served to veto electrons in the beam. Polyethylene was used as a moderator to remove pions and to slow down the muons.

The diode was surrounded by a split NaI(Tl) annulus, 5 in. long with inner and outer diameters of $2\frac{3}{4}$ and $7\frac{1}{4}$ in. It was split on a diameter giving it two optically isolated halves. Each half was viewed by two RCA 6342 photomultipliers. This arrangement was operated in two modes simultaneously. One mode was with both annulus halves in anticoincidence with the diode, the other was with each half and the diode in coincidence. The former mode was used to reduce the Compton continuum under the full-energy peaks. The latter mode, useful only at energies above 2 MeV, was used to reduce the Compton events under the double-escape peaks by requiring events in the diode to have one annihilation quantum in each half of the annulus.

B. Spectrometer

The spectrometer proper was made up of the diode, preamplifier, amplifier, analog-to-digital converter (ADC), digital stabilizer together with two fixed pulsers, and a variable pulser whose amplitude was monitored by a digital voltmeter. These elements are shown in Fig. 2.

The diode, a 17 cm^3 pure-coaxial type, 2.8-cm o.d. and 3.1 cm long, was lent to us by AECL, Chalk River Nuclear Laboratories. It had a resolution of 2.5 keV at 100 keV and 4.5 keV at 1.3 MeV, making use of a Tennelec TC 130 preamplifier modified to provide cooling of the input field-effect transistor. The preamplifier resolution was 1.0 keV under zero-capacitance conditions. Its decay time constant was 35 μsec .

The amplifier was a Tennelec TC 200. Under most conditions, it was used with both first differentiating and integrating time constants set at 3.2 μsec and without a second differentiation.

The output from the amplifier was fed into a linear gate which was opened by a coincidence between the diode and the telescope. The height of the pulse from the output of the linear gate was digitized and fed to an on-line PDP-8 computer.

The ADC was regulated by two digital stabilizers.⁷ One, set near channel 500 regulated the zero level of the ADC. The other was set near channel 3500 and regulated the gain. The stabilizers were gated to accept only pulses from the two fixed pulsers. These were mercury relay pulsers with a power supply using Zener reference diodes stable to 5 parts per million per degree C. They were driven at ~ 50 cps, out of synchronism with the line frequency. The pulser outputs were fed into the system at the input of the preamp in parallel with the diode. The voltages on the pulsers' storage capacitors were monitored every 20 min by a digital voltmeter to check for drifts.

A 20-position stepping pulser was also fed into the system. It was used to monitor the stability and to correct for the nonlinearities of the spectrometer. Its power supply was the same as that mentioned above, with the addition of a precision divider chain tied to a

⁷ J. A. Ladd and J. M. Kennedy, Atomic Energy of Canada, Ltd. Report No. 1417, 1961 (unpublished).

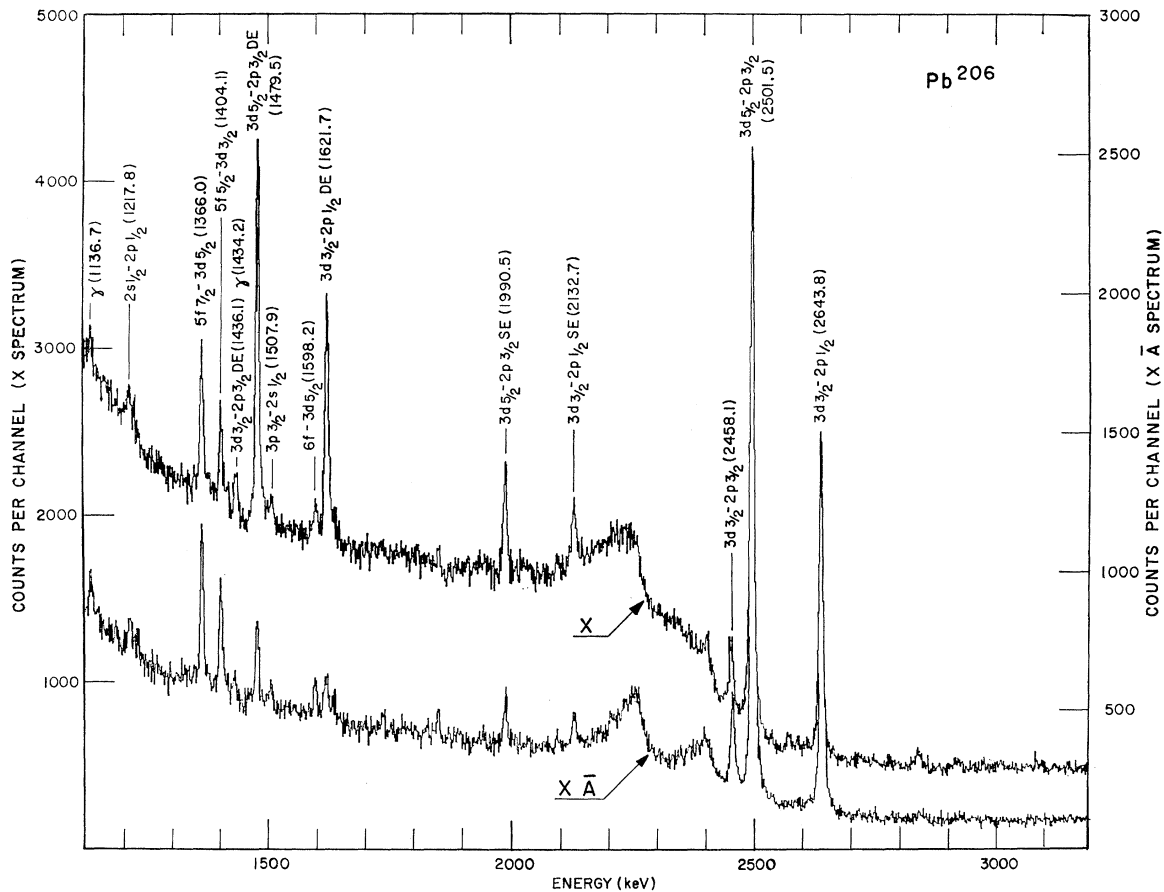


FIG. 5. Intermediate-energy region of prompt spectrum in Pb^{206} . The X spectrum contains all prompt events, the X \bar{A} spectrum the prompt events in anticoincidence with the NaI annulus.

20-position Au-contact stepping switch to produce a series of voltages on the capacitor. Six hundred pulses were fed into the system at each stepping-switch position. The voltage on the capacitor at each position, with the mercury relay turned off, was measured by a digital voltmeter before and after feeding the pulses into the ADC and recording them in the computer.

C. Logic Circuitry

The logic circuitry will not be described here in detail. It was built up mainly from E.G.G. logic modules in a standard way. However, four special devices were incorporated: (i) an extendable deadtime inspector, (ii) a rate detector, (iii) a standard γ -ray source system, and (iv) an annulus circuit.

The inspector was a circuit which vetoed any input pulse when another pulse preceded it within 50 μsec . This was introduced to ensure that the tail from a previous pulse would not perturb the pulse under study.

The rate detector was an up-dating one-shot which was fired by a (1, 2) coincidence in the telescope. The one-shot kept itself on while the beam was on and turned itself off during the beam offtime. It was used as

a gate, so that input pulses which were uncorrelated with the beam would be measured only during beam-on conditions and would therefore suffer the same distortions due to rate effects as the x rays.

The standard γ -ray sources were brought in gated by the inspector, the rate detector, and a pulse-height discriminator set just below 511 keV. They were vetoed by a (1, 2) telescope event. Thus, all events above 480 keV and not in coincidence with the telescope were analyzed by the ADC as source events. However, only those events in regions of the source peaks were stored in the computer, which handled five regions of 50 channels each. The standard sources increased the singles rates in the diode by about 15%, to about 3500 events per second, and therefore caused little additional distortion due to rate effects.

The annulus circuit is shown in Fig. 3. The clipping of the anode output by the dynode pulse should be noted. This was done to reduce the dead time of the system due to large pulses. The scintillator can absorb a large fraction of high-energy background radiation which goes up to 100 MeV or more. If one works with the current pulse, such large pulses decay with the

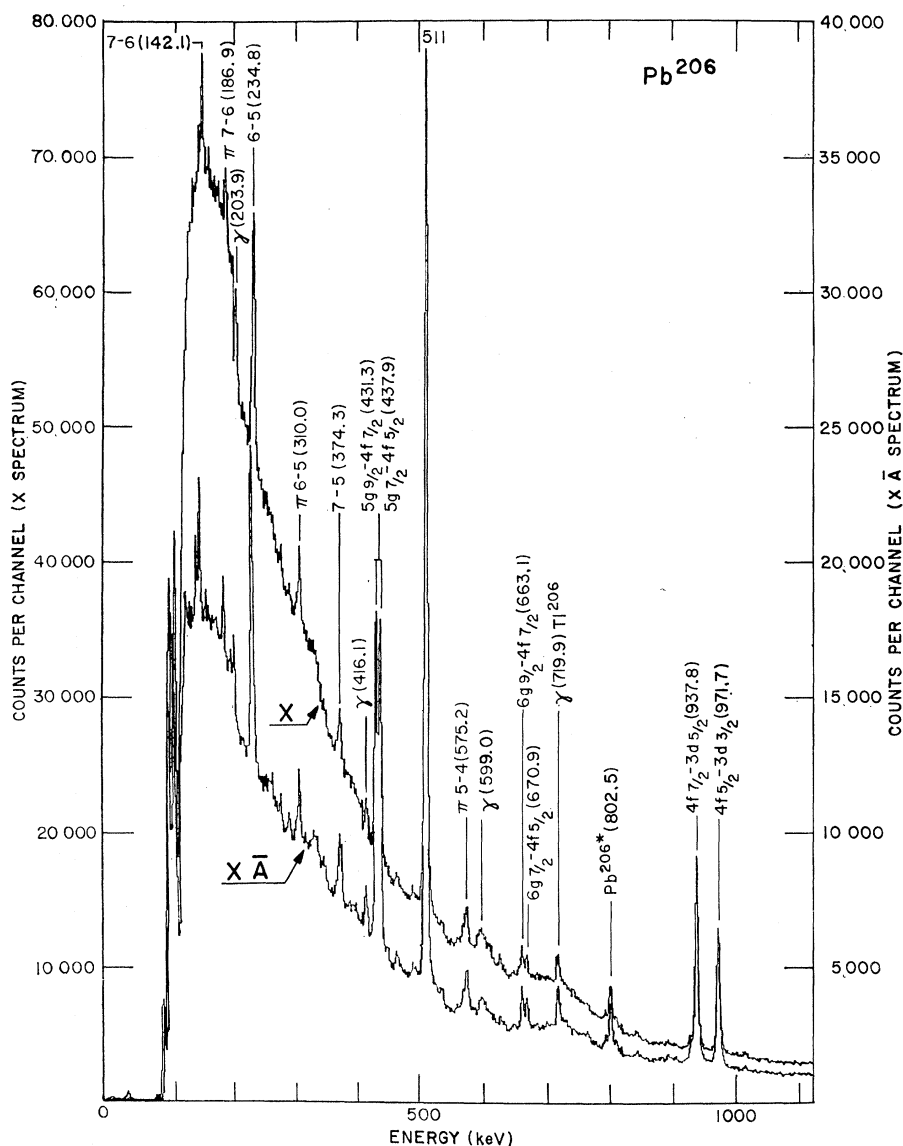


FIG. 6. Low-energy end of the prompt spectrum in Pb^{206} . The X and $X\bar{A}$ spectra are defined as in Fig. 5.

scintillator decay time of $0.25 \mu\text{sec}$ and have to drop by a factor of 200 or more before the current is reduced to the size of the pulses which are of interest. Without clipping, this could take more than $1 \mu\text{sec}$. Moreover, the early stages in the amplifier system could be overloaded, and since the counting rate in a half annulus was about 10^9 counts/sec, there could be appreciable losses after large pulses.

To get around these problems, the dynode current pulse was used to clip the anode current pulse. These pulses have identical time-decay characteristics, that of NaI(Tl) , but are opposite in phase. Thus, if the dynode output is delayed until its initial amplitude just equals that of the anode output, and if it is added to the anode pulse the two pulses will cancel except for statistical fluctuations. This will restore the base line for the entire length of the pulse.

The best value of the delay (δ) was found to be 85 nsec. Now $\delta = \tau \ln[m/(m-1)]$, where τ is the decay time of scintillator, m is the multiplication factor of dynode 10. If $\tau = 250$ nsec, then m turns out to be 3.5, which is reasonable.

D. Timing

The main timing of the system was done digitally and therefore deserves some special attention. Since the operating range of the pulse heights was 60:1, it was difficult to construct a system which would give precise timing over the whole range. The method devised made use of the on-line computer system and was feasible because of the relatively low rates.

The time of arrival of the Ge-diode discriminator pulse relative to the telescope pulse was digitized by an Eldorado interval timer and fed to the computer as

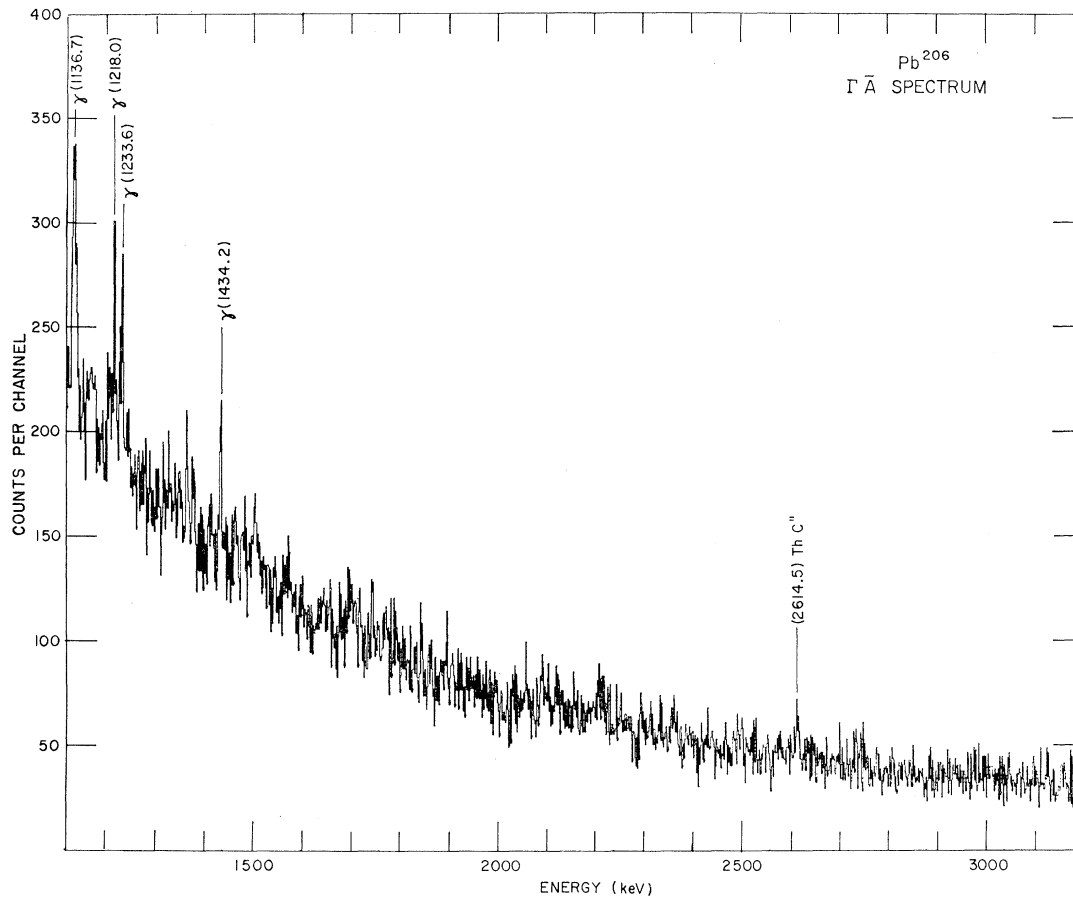


FIG. 7. Intermediate-energy region of delayed spectrum in anticoincidence with the NaI annulus, for Pb²⁰⁶.

shown in Fig. 2. The stop pulse came from a trigger set to fire on Ge pulses above 35 keV. The distribution of interval timer outputs was then measured as a function of energy. Using this information, prompt and delayed windows for each 128-channel interval of pulse height were selected and stored in the PDP-8. The computer examined the height and time of each pulse to decide whether an event was prompt or delayed. This method gave a variable but measurable resolution over the whole region and made it possible to calculate the μ -capture γ -ray contribution to the prompt spectrum. The time resolution varied from 80 nsec at 100 keV to 10 nsec at 6.0 MeV, but most of the change occurred before 0.5 MeV, where the resolution was better than 30 nsec. The delay of the prompt peak also changed by 68 nsec over the useful range.

E. Computer System

The computer system, as indicated in Fig. 2, was made up of two computers, a PDP-8 with a capacity of 8192 12-bit words, and an ASI 6040 with 16 384 24-bit words. Four thousand PDP-8 words were used for on-line control of the peripheral measuring equipment and sorting of the data from it. The remaining 4000 words

were used for storage. The ASI was used for data storage and for checking the stability of the spectrometer.

The PDP-8 controlled the two pulsers and the digital voltmeter. It turned the pulsers on and off in a regular way during normal data acquisition and measured the voltage on the charging capacitors with the digital voltmeter. The sequence was as follows: With the stepping-pulsers mercury switch turned off, the computer read the voltage on the pulser's capacitor, turned the mercury relay on, and kept it on until 600 pulses had been stored, turned the relay off, and finally, recorded the voltage again. The computer then stepped the pulser on to the next position. This sequence was repeated for all 20 positions. After the last pulser position, the zero of the digital voltmeter was read. Finally, the two stabilizer pulsers were turned off and their voltages read in turn. The values of their voltages were checked against the reference values, near 1.0 and 7.0 V, and if the shift was more than 1.0 mV, the system was stopped and checked. This whole cycle ran continuously with a period of about 20 min in parallel with the data acquisition.

The PDP-8 computer received information from the

logics, the ADC, and the interval timer, and used it to decide where to store the data. Each pulse measured by the ADC had associated with it a delay-time reading from the interval timer and a tag-resister reading. The tag resister was used to identify the type of event measured, i.e., target 1 or 2, calibration of source, or pulser, as well as the response of the annulus. Using this information, the PDP-8 stored the data in five types for each target. These were for the prompt events, all data (X), data in anticoincidence with the annulus ($X\bar{A}$), and data in coincidence with both

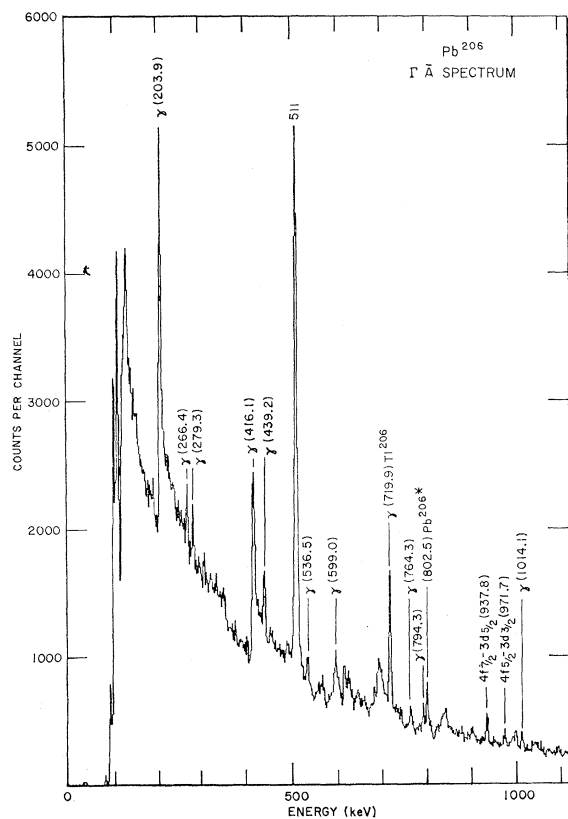


FIG. 8. Low-energy region of the delayed spectrum in anticoincidence with the NaI annulus, for Pb^{206} .

halves of the annulus ($X\bar{A}$); for the delayed events, ($\Gamma\bar{A}$) and (ΓA), but not (Γ). Also, the pulser and source data were tagged and stored. The X spectra were stored for channels 0–4096 the $X\bar{A}$ and $\Gamma\bar{A}$ spectra for channels 0–2047 and the $X A$ and ΓA spectra for channels 1296–4095. This used up 27 584 memory locations. The Γ spectra were not recorded because of lack of space.

The PDP-8 was operated on a program-interrupt basis. It was interrupted by the ADC, the digital voltmeter, or the stepping of the pulser. When an ADC interrupt occurred, the interrupt was turned off and the contents of the ADC, the interval timer, and the tag register were stored in a temporary buffer;

TABLE I. Line-shape parameters for the principal lines of Pb^{206} .

Line	Approximate energy (keV)	E (FWHM) (keV)	$E_{1/2}$ (keV)	f_1
$3d \rightarrow 2p$ (DE)	1500	6.4	5.6	0.44
$3d \rightarrow 2p$ (SE)	2000	7.2	5.6	0.61
$3d \rightarrow 2p$ (FE)	2500	7.8	3.3	0.44
$2p \rightarrow 1s$ (DE)	4800	9.2	5.4	0.76
$2p \rightarrow 1s$ (SE)	5300	9.4	6.1	0.84
$2p \rightarrow 1s$ (FE)	5800	8.9	5.1	0.87

then the interrupt was turned back on. A digital-voltmeter interrupt was treated similarly with the reading being stored in the temporary buffer with a suitable tag. The stepping-switch interrupt was used to continue on to the next step in the pulser cycle.

The period between interrupts was used by the computer to process the data in the temporary buffer. Each event in the buffer was sorted into one of the previously described 10 data spectra, a source or pulser spectrum. The source events and some of the data events were stored in the PDP-8. A four-bit tag word was then added to the other data and these two words were placed in a transfer buffer in preparation for transmission to the ASI. When it was filled, the contents of this 32-word buffer were transferred to a buffer in the ASI. These data were used by the ASI to update the appropriate locations in its spectra. In all, 23 488 storage locations were required in the ASI. This was obtained by breaking 11 744 24-bit words into twice that number of 12-bit words.

The pulser and associated digital-voltmeter data were used by the ASI to check the stability of the system. Each pulser peak was composed of 600 events and an associated pair of digital-voltmeter readings. The position of each peak was found by fitting it to a gaussian by use of a method of least squares. These results were then used to determine, by a method of least squares, the coefficients of the polynomial,

$$V = b_{-1}C^{-1} + b_0 + b_1C + b_2C^2,$$

relating the digital-voltmeter readings to their associated pulser-peak positions in channels C .

TABLE II. Constitution of targets.^a

Pb target	Thickness (g/cm ²)	Pb^{206} (%)	Pb^{207} (%)	Pb^{208} (%)
206	8.1	88.72	8.48	2.73
207	7.63	2.16	92.40	5.48
208	8.12	0.20	0.05	99.75
Nat. Pb	8.09	24.93	21.39	52.31
Nat. Pb	4.05	24.93	21.39	52.31
Nat. Pb	1.96	24.93	21.39	52.31

^a Pb^{204} makes up the rest of the isotopic impurity in each target.

TABLE III. Calibration energies and fit.

γ source	Literature (keV)	Fit mean value (keV)	Fit rms deviation (keV)
511-keV line	511.01 ± 0.00	511.01	0.04
ThC''	2614.47 ± 0.10^a	1592.46 DE 2614.48 FE	0.24
Na ²⁴	2753.92 ± 0.12^a	1731.87 DE 2753.89 FE	0.13
O ¹⁶ *	6129.96 ± 0.46^b	5108.09 DE 6130.11 FE	0.19

^a G. Murray, R. L. Graham, and J. S. Geiger, Nucl. Phys. **63**, 353 (1965).

^b C. Chasman, K. W. Jones, R. A. Ristinen, and D. E. Alburger, Phys. Rev. **159**, 830 (1967).

III. Pb²⁰⁶ X-RAY AND γ -RAY SPECTRA

In this section, we illustrate the output from the system with the data taken on Pb²⁰⁶ and show some of the new features which appeared. Since Pb²⁰⁶ was used as the reference target in our two-target system, a large amount of Pb²⁰⁶ information was collected during the course of the experiment. Those data were analyzed by individual runs but summed together in order to observe weak transitions. The spectra shown in Figs. 4–8 are from about one-half the Pb²⁰⁶ data taken over a period of two months and added channel by channel. The resolution deteriorated by less than one channel by this procedure, indicating the high stability of the system over long periods.

The high-energy end of the prompt spectrum, events in which the diode was in prompt coincidence with a muon stop, is shown in Fig. 4. This exhibits the typical features of a Ge diode x-ray spectrum. The $2p$ - $1s$ transitions appear as a pair of peaks in the X spectrum three times. The full-energy (FE) peaks appear at the upper end of the spectrum, the single-escape (SE) peaks appear quite clearly 511.01 keV lower, and the double-escape (DE) peaks appear most distinctly 1022.02 keV lower. The $X\bar{A}$ spectrum is plotted for comparison below the X spectrum. In $X\bar{A}$ the requirement that there be a coincidence with one annihilation γ ray in each half of the annulus selects out the DE peak and suppresses the SE and FE peaks. This feature helps

TABLE IV. Energy differences used for calibration.

Pb line	Lower peak	Upper peak	Energy difference (keV)
$3d_{5/2}-2p_{3/2}$	SE	FE	511.01
$3d_{3/2}-2p_{1/2}$	SE	FE	511.01
$2p_{1/2}-1s_{1/2}$	DE	SE	511.01
$2p_{1/2}-1s_{1/2}$	DE	FE	1022.02
$2p_{3/2}-1s_{1/2}$	DE	SE	511.01
$2p_{3/2}-1s_{1/2}$	DE	FE	1022.02

determine which peaks are DE, and hence with 1022.02 keV less than their full energy, and which are FE peaks. Thus, the peak at 3429 keV is identified as a FE peak from the $4d_{5/2}-2p_{3/2}$ transition by its absence in the $X\bar{A}$ spectrum. A comparison of the X and $X\bar{A}$ spectra shows that the efficiency of detection of the escaping pairs is high, approximately 40%. The reduction of the continuum by a factor of 10 results in an improvement in the net signal-to-background ratio by a factor of 4.

The middle-energy region is shown in Fig. 5. Here the $3d$ - $2p$ transitions which are split by the spin-orbit interaction into a triplet of lines also appear three times as FE, SE, and DE peaks. In this case, the FE peaks are most prominent, although the SE and DE peaks are clearly in evidence. The lower spectrum this time is the $X\bar{A}$ spectrum which selects those events in which there is no γ ray in the annulus in coincidence with the Ge pulse. This combination suppresses the DE and the

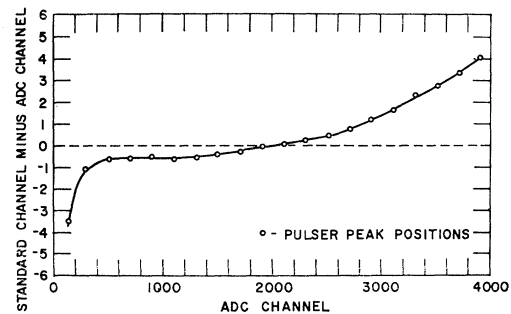


FIG. 9. Nonlinearity of the system as measured with the standard pulser peaks.

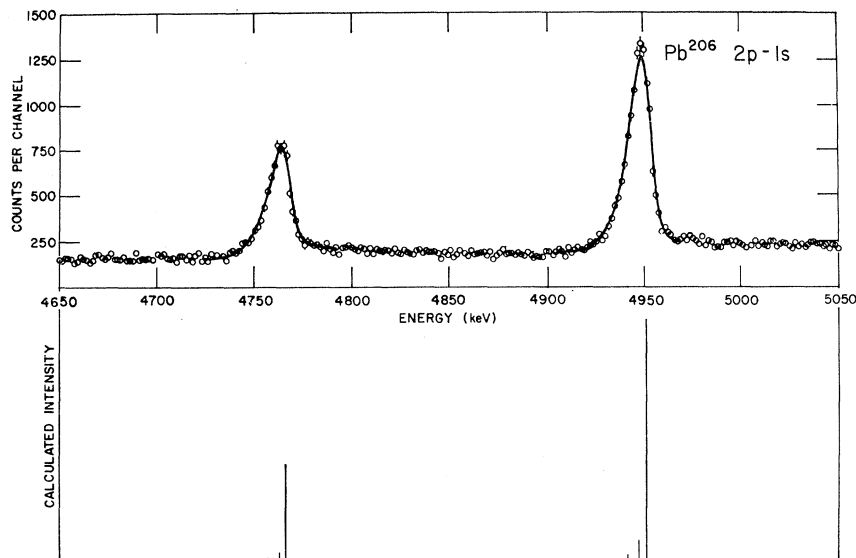
SE peaks, and even though the suppression is not complete, it becomes quite easy to tell which of the peaks are FE and which are DE and SE. The $X\bar{A}$ spectrum has a 4-times-lower Compton background. The signal-to-background ratio in the $X\bar{A}$ spectrum is seen to be about 2 times better than in the X spectrum.

A disadvantage of the $X\bar{A}$ mode is that it tends to suppress the desired events. This comes about because each x ray is part of a cascade of x rays, any of which might trigger the anticoincidence. If the NaI annulus were efficient enough, no x ray would be recorded in this mode. This makes the $X\bar{A}$ mode unreliable for intensity measurements.

Some of the weaker lines are evident in this part of the spectrum. In particular, the higher terms of the Paschen series ($nf \rightarrow 3d$) appear near 1.4 and 1.6 MeV. The lines corresponding to $2s_{1/2}-2p_{1/2}$ (1218 keV) and $3p_{3/2}-2s_{1/2}$ (1508 keV) play a special role in the analysis of the nuclear charge distribution. The line at 1137 keV is identified as a capture γ ray because of its appearance in the $\Gamma\bar{A}$ spectrum.

The low-energy part of the spectrum is shown in Fig. 6. Here again the X and the $X\bar{A}$ spectra are shown together. The principal transitions, $4f-3d$ and $5g-4f$,

FIG. 10. Example of line-shape fit of the $K\alpha$ lines from the Pb^{206} target. The vertical bars in the lower half of the figure indicate the calculated positions and relative contributions of the three Pb isotopes present.



appear quite prominently and are adequately resolved for a clear identification. The line at 235 keV is due principally to the $6h-5g$ transitions, but the triplet of lines are not resolved in this case. Moreover, additional $6-5$ transitions such as $6g-5f$ contribute. A similar situation obtains at 142 keV for the $7-6$ transitions.

We have assigned some of the lines to π x rays, an indication that the separation from pions was not complete. The capture γ -ray lines are identified because of their appearance in the delayed ΓA spectra.

The delayed ΓA spectra of Figs. 7 and 8 show almost exclusively the μ -capture γ rays. These show up in the X and $X A$ spectra as well, with an intensity determined by the width of the time window used for identifying prompt events. More detail about the intensities of the lines seen here is given in Sec. VIII.

We do not show the ΓA spectrum taken in the region 3.2–6.5 MeV. This region is remarkable for its lack of structure, with no evidence for capture γ rays. The only peak is the 6.130 MeV DE line due to O^{16*} from our neutron-irradiated water source, which appears in the delayed spectrum by accidental coincidence, made appreciable here by the wide time acceptance used in the delayed spectrum.

IV. DATA REDUCTION

A. Peak Fitting

The positions of the peaks in these spectra were found by fitting to the data an empirical line shape which expresses the idea that the basic response of the apparatus is Gaussian and that there is a low-energy exponential tail due to the presence of some regions of inefficient charge collection.

Our assumed mathematical line shape thus consisted of an unperturbed Gaussian part plus a part in which

the same Gaussian is modified by a low-energy exponential tail. Letting $N_p(C)$ be the number of counts in channel C due to the peak centered on channel C_0 , we write

$$N_p(C) = N_0 \left(f_1 \beta \int_C^\infty \exp[-\lambda(C'-C_0)^2 - \beta(C'-C)] dC' + (1-f_1) \exp[-\lambda(C-C_0)^2] \right), \quad (1)$$

where $1-f_1$ is the fraction of the counts in the pure Gaussian part while f_1 is the fraction in the asymmetric part. The amplitude parameter N_0 is related to the intensity of the peak by

$$I = N_0 (\pi/\lambda)^{1/2}. \quad (2)$$

This result comes directly from our choice of normalization of the two terms of Eq. (1).

The width parameter of the Gaussian λ and the asymmetry parameter β can be written in terms of energy. Let ξ be the energy per channel. Then the full width at half-maximum of the Gaussian $E(\text{FWHM})$, and the decay constant of the folded-in exponential $E_{1/2}$, are related to λ and β by

$$E(\text{FWHM}) = 2\xi(\ln 2/\lambda)^{1/2}, \quad (3)$$

$$E_{1/2} = \xi \ln 2/\beta. \quad (4)$$

Our fits to the peaks are in terms of $E(\text{FWHM})$ and $E_{1/2}$. Note that, for $f_1 \neq 0$, $E(\text{FWHM})$ is smaller than the FWHM of the observed peak because of the low-energy tail.

To provide a reasonably complete description of the data, background terms must be added to Eq. (1). Let $N_b(C)$ be the number of counts in the background at channel C . We have chosen the following description

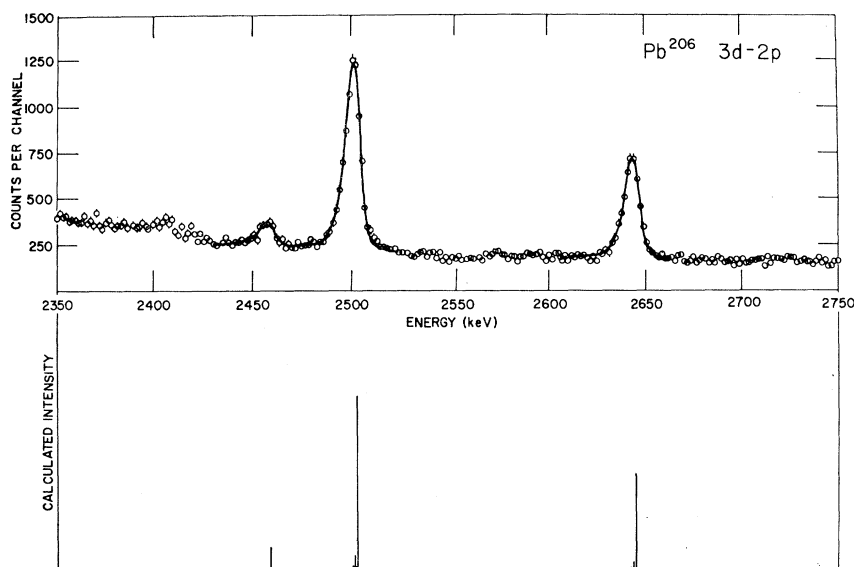


FIG. 11. Example of the line-shape fit of the $L\alpha$ lines from the Pb^{206} target. The calculated relative intensities of the three lines are shown by the vertical bars. The separation of Pb^{207} and Pb^{208} impurities are too small to show clearly.

for the background:

$$N_b(C) = U + V(C - C_1) + N_0 \left(f_2 \lambda^{1/2} \int_{-\infty}^C \exp[-\lambda(C' - C_0)^2] S(C - C') dC' + f_3 \int_C^{\infty} \exp[-\lambda(C' - C_0)^2] dC' \right), \quad (5)$$

where C_1 is the starting channel in the region of fit, which is chosen to include a sizable portion of the background. The f_3 term is a Compton-scattering background used only in DE and SE peaks. It takes care of the extra energy left by those escaping 511-keV annihilation quanta that Compton-scatter before leaving the Ge detector. The function $S(C - C')$ is proportional to the Compton-scattering cross section. The f_3 term takes care of the case of FE peaks, which always have a higher background on the low-energy side due to multiple Compton scattering of the γ rays of the peak energy.

When several fairly closely spaced peaks were fitted simultaneously, the same peak-shape parameters, λ , β , and f_1 , and the same background parameters, f_2 and f_3 , were used for all the peaks. Each peak had its own position and amplitude parameters C_0 and N_0 , which were determined by the fit. Furthermore, where groups of separated peaks or groups of peaks from different runs were simultaneously fitted, each group was given its own background parameters U and V .

Using Eqs. (1) and (5), a typical fit to a section or sections of the spectra was made by allowing the parameters to vary until a minimum χ^2 was obtained. The variation of χ^2 about the minimum gives the errors on the parameters, including the error on the position parameter C_0 . In general, reasonably good χ^2 values were obtained for the fits and a smooth average varia-

tion of $E(\text{FWHM})$, $E_{1/2}$, and f_1 as functions of channel number were obtained. Representative values are given in Table I.

In the final analysis, however, the position parameter of the Gaussian C_0 was not used to define the peak position. Rather, the position of the top of the fitted line shape where $dN_p(C)/dC = 0$ was chosen. The reason for this was that although the mathematical form of our line shape, Eq. (1), is reasonable, it is not an exact description of the peaks. The value of χ^2 does not have a uniquely defined sharp minimum as a function of the parameters that go into Eqs. (1) and (5). It can be rather broad and may have many small local minima. If the same peak is fitted several times, several sets of parameters may be found, each fitted equally well. In some cases, different fits to the same peak would give a differing C_0 by as much as 1.5 keV without

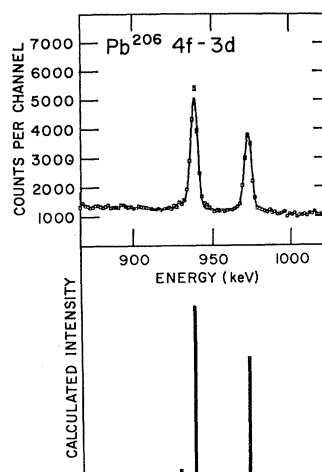


FIG. 12. Example of the line-shape fit to $M\alpha$ lines in Pb^{206} and calculated relative intensities.

much change in χ^2 . The position of the top of the fitted peak was found to be much less sensitive to the details of the method employed. This is because the top of the peak is a property of the data and should be relatively independent of the functional form used, while C_0 depends on the particular function used in the fit. For the error in the peak position, we took, for simplicity, the error found for C_0 .

The peak positions were corrected to allow for the nonlinearities in the electronics. Between channel 300 and 4000 this nonlinearity amounted to one part in 1000. The corrections were made using the channel positions of the 20 pulser peaks and their corresponding DVM readings. The observed channels were converted to a standard linear set by referring to the DVM readings. Let C_i be the measured ADC channel of the i th pulser peak. The standard channel of the pulser peak C_i^s is defined as the corresponding DVM measurement V_i , scaled by a factor designed to preserve essentially the channel width in going from ADC channels to standard channels;

$$C_i^s = (V_i/V_{10})C_{10}, \quad (6)$$

where C_{10} and V_{10} refer to the tenth pulser peak located near the center of the 4096-channel ADC range. Any measured x-ray or γ -peak was converted from its ADC channel to the standard channel by the four-point Lagrangian method using the four nearest values of C_i and C_i^s .

A sample plot of the deviation of the ADC channel from the standard channel is shown in Fig. 9 over the whole range of the ADC for a series of 11 runs that were taken at a gain of 1.6 keV/channel. As a result of changes made in the settings in the electronics, six such curves were obtained for the whole experiment (which lasted three months), but only two differed noticeably among the curves for the low-gain (1.6-keV/channel) data. One single curve served for all the high-gain (0.4-keV/channel) data. The deviation was smooth and small except at the low-channel end. Between channel 300 and 4000 it never exceeded four channels or 1 part in 1000. For the gain setting of 0.4 keV/channel, it was even less, namely, 1.5 channels in 4000.

TABLE V. Calibration lines in Ra²²⁶ source.

Line	Energy (keV)
Ra186 (Rn ²²² *)	186.00±1.00 ^a
Ra242 (Bi ²¹⁴ *)	241.92±0.03 ^b
Ra352 (Bi ²¹⁴ *)	351.99±0.06 ^b
Ra609 (Po ²¹⁴ *)	609.40±0.10 ^a
Ra1120 (Po ²¹⁴ *)	1120.40±0.10 ^a

^a Nuclear Data Group, Nuclear Data 1, No. 5 (1966).

^b D. E. Muller, H. C. Hoyt, D. J. Klein, and J. W. M. du Mond, Phys. Rev. 88, 755 (1952).

TABLE VI. Examples of the energy-calibration coefficients.

	a_0 (keV)	a_1 (keV/channel)	a_2 (10 ⁻⁸ keV/ channel ²)
Low gain	3.21±0.15	1.60040±0.00025	-0.140±0.071
High gain	1.23±0.15	0.39114±0.00020	-0.071±0.064

B. Data Analysis

Throughout most of the experiment, the Pb²⁰⁶ target was chosen as one of the two targets. It served as a standard against which the other targets were measured. The Pb²⁰⁶ target was chosen because this isotope is readily available in quantity and because its muonic transitions have a simple line structure. Thus, large amounts of data were obtained for it compared to the other targets; this made it possible to measure the Pb²⁰⁶ principal transitions very precisely. Five other Pb targets were also used during the experiment: three natural-Pb targets, one of Pb²⁰⁷, and one of Pb²⁰⁸. The three targets of separated Pb isotopes were relatively pure; Table II gives the isotopic composition of each target and its dimensions.

The data taken at low gain, 1.6 keV/channel, covering an energy range 100–6400 keV, were analyzed as a collection of 11 summed spectra. Nine were for Pb²⁰⁶, one was for Pb²⁰⁷, and one was for Pb²⁰⁸. In a summed spectrum, the data of several runs were added channel by channel. Because of the very good stability, no shifting or stretching of channels was necessary. Each summed spectrum consisted of the sum of twenty individual runs. How the individual Pb runs were grouped for summing was dictated by the second target. For example, in ten successive runs, different combinations of the three Pb isotopes were used in the two target positions. Out of these ten runs, three summed spectra, one of Pb²⁰⁶, one of Pb²⁰⁷, and one of Pb²⁰⁸ were made. In other cases, the second target was a different element such as La, Au, Th, etc.

The Pb x-ray lines in the 11 summed spectra were analyzed by fitting them with the mathematical peak shape of Eq. (1). The principal transitions, from $2p$ - $1s$ to $5g$ - $4f$, with a few exceptions, were included in the analysis. The DE, SE, and FE peaks of the K and L lines were analyzed except for the SE $3d_{3/2}$ - $2p_{1/2}$ transitions in three of the summed runs and the DE and SE $3d_{3/2}$ - $2p_{3/2}$ transitions in all of the runs. These were too weak for a reliable analysis.

Because of the presence of Pb²⁰⁷ and Pb²⁰⁸ in the Pb²⁰⁶ target, the Pb²⁰⁶ K and L lines were analyzed by fitting to each line three components described by Eq. (1) with the amplitude of each proportional to the isotopic abundance and spaced by the isotope shift obtained from the measurements with Pb²⁰⁷ and Pb²⁰⁸. Also, in fitting the K and L lines, the shape parameters were kept at the values listed in Table I.

TABLE VII. Principal lines and fine-structure splittings in Pb²⁰⁶.

Transition	Acker <i>et al.</i> ^a (keV)	Anderson <i>et al.</i> ^b (keV)	Powers ^c (keV)	This experiment (keV)
$2p_{3/2}-1s_{1/2}$	5972.3±5.0	5979.7±5.2	5974.1±2.0	5973.98±0.44
$2p_{1/2}-1s_{1/2}$	5786.9±5.0	5792.1±5.0	5789.0±2.0	5788.33±0.48
$3d_{3/2}-2p_{1/2}$	2643.2±3.0	2645.1±1.9	2645.5±2.3	2643.75±0.36
$3d_{5/2}-2p_{3/2}$	2500.6±1.5	2502.8±1.8	2503.4±2.3	2501.45±0.43
$3d_{3/2}-2p_{3/2}$				2458.10±0.38
$4f_{5/2}-3d_{3/2}$	969.1±2.6	970.7±1.7		971.74±0.20
$4f_{7/2}-3d_{5/2}$	933.7±2.4	937.2±1.7		937.76±0.20
$5g_{7/2}-4f_{5/2}$				437.86±0.15 ^d
$5g-4f$	435.2±1.2 ^e			
$5g_{9/2}-4f_{7/2}$				431.25±0.12 ^d
$6h-5g$	235.6±1.6 ^e			234.59±0.19 ^{d,e}
Splitting				
Δp (<i>K</i> lines)	185.4±2.0	187.6±1.4	185.1±2.0	185.65±0.12
$\Delta p-\Delta d$ (<i>L</i> lines)	142.6±2.5	142.3±1.4		142.30±0.24
Δd (<i>L</i> lines)				43.47±0.44
$\Delta d-\Delta f$ (<i>M</i> lines)				33.98±0.10
$\Delta f-\Delta g$ (<i>N</i> lines)				6.61±0.20

^a Reference 8.^b Reference 3.^c Reference 9.^d Includes data from Pb²⁰⁷ and Pb²⁰⁸.^e Center of gravity of the triplet.

A typical fit in the case of the $2p-1s$ (DE) transitions in Pb²⁰⁶ is shown as the solid line in Fig. 10. The contribution of the three isotopes present in the target is indicated in the figure. Fits for the $3d-2p$ (FE) and the $4f-3d$ (FE) transitions are shown in Figs. 11 and 12, respectively.

For the $4f-3d$ and higher transitions the isotope shift was ignored, although there was some indication of a small (~ 0.05 -keV) isotope shift in the *M* lines. Thus, the higher transitions of all four targets of Pb were analyzed in the same way: that is, only one component was fitted to each fine-structure peak. The final results for the low-gain data are averages over all three isotopes. Since the peaks of the higher transitions were nearly Gaussian, the shape parameters were varied in each case to obtain the best fit. The $5g$ fine-structure splitting was fixed at its theoretical point-nucleus value of 2.78 keV in fitting the $5g-4f$ transition. The 511-keV annihilation line appearing in all the *X* spectra was analyzed and used in the absolute-energy calibration.

In the high-gain (0.4-keV/channel) data, whose range was 70–1600 keV, the spectra from four individual runs were analyzed. Both targets in the four runs consisted of different thicknesses of natural Pb. The principal transitions from $4f-3d$ to $6h-5g$ as well as the 511-keV peaks were analyzed in the manner described above.

For both the high- and low-gain data, the *X* spectra were used in the energy calibrations, isotope shifts, and intensity ratios. For comparison, some of the *K* lines

in the *XA* spectrum and *L* lines in the $X\bar{A}$ spectrum were also analyzed. The reduced background in the *XA* and the $X\bar{A}$ spectra makes analysis less sensitive to the background subtraction. No discrepancies outside of statistics were found in comparing the results for the same lines in the different spectra.

C. Energy Calibration

The calibration was done using a quadratic

$$E = a_0 + a_1C + a_2C^2, \quad (7)$$

where now *C* stands for the standard channel of the peak position. The *E-C* coefficients, a_0 , a_1 , and a_2 , for a typical low-gain Pb²⁰⁶ summed spectrum were obtained by a least-squares fit to Eq. (7). Data peaks were used, for which either the energies or the energy differences with respect to other peaks were known. We took advantage of the precisely known energy differences between the DE, SE, and FE peaks of the same transition. These differences supplemented the data from standard γ -ray sources of well-known energies.

The source peaks were analyzed in the same way as x-ray peaks in order to extract their standard channel positions in a consistent manner. In the low-gain runs, the DE and FE peaks of one of the γ rays of Na²⁴ and of O^{16*} from a neutron-irradiated water source were used. The Na²⁴ line is quite close to the Pb²⁰⁶ *L* lines while the O^{16*} line is close to the Pb²⁰⁶ *K* lines. One of the Th γ -ray lines (ThC'') was used instead of the Na²⁴ line for the summed spectrum in which Th²³² was the second

TABLE VIII. Isotope-shift measurements.

Transition	IS(206–207)	IS(206–207)	Standard shift (keV)	This expt	IS _{obs} /IS _{std}	
	Powers ^a (keV)	This expt (keV)			Optical Steudel ^b	Electron x ray Chesler and Boehm ^c
$2p_{3/2}-1s_{1/2}$	3.72 ± 0.32	4.30 ± 0.10	8.03	0.54 ± 0.01	0.46 ± 0.07	
$2p_{1/2}-1s_{1/2}$	4.02 ± 0.86	3.59 ± 0.10	7.62	0.47 ± 0.01		
$3d_{3/2}-2p_{1/2}$	1.31 ± 0.58	1.50 ± 0.18	1.24	1.21 ± 0.15		
$3d_{5/2}-2p_{3/2}$	0.54 ± 0.62	0.59 ± 0.11	0.86	0.69 ± 0.13		
	IS(206–208)	IS(206–208)				
$2p_{3/2}-1s_{1/2}$	9.36 ± 0.30	10.21 ± 0.10	15.96	0.64 ± 0.01	0.60 ± 0.07	0.56 ± 0.08
$2p_{1/2}-1s_{1/2}$	9.27 ± 0.89	9.40 ± 0.15	15.18	0.62 ± 0.01		
$3d_{3/2}-2p_{1/2}$		2.27 ± 0.22	2.47	0.92 ± 0.09		
$3d_{5/2}-2p_{3/2}$		1.38 ± 0.14	1.72	0.80 ± 0.08		

^a Reference 9.^b Reference 37.^c Reference 38.

target. The Th C'' γ ray is also close in energy to the Pb²⁰⁶ L lines. In addition, the 511-keV γ ray from positron annihilation in the water source was collected in the same way as the other standard γ rays. Table III lists the sources used for the energy calibration in the low-gain data, together with the mean value and standard deviation of the fit obtained.

In the low-gain sums, the precisely known energy differences between the FE, SE and DE peaks for the K and L lines were also used to determine the coefficients in Eq. (7). Table IV summarizes the differences used. The DE Pb²⁰⁶ L lines were not used because of a local nonlinearity in the electronics. For the K lines, the DE peaks were used in both differences because these are stronger than either the SE or FE peaks.

For the high-gain data, only absolute energies were available, since the lowest energies capable of having the DE, SE, and FE peak differences were above the range of the ADC. In this case, five lines from a natural Ra²²⁶ source were used, as listed in Table V. In addition, the 511-keV annihilation γ ray appearing in both of the natural-Pb spectra was available and was used in the calibration.

Two examples of the energy-calibration fit, one high-gain, the other low-gain, are shown in Table VI. The

average value of χ^2/N for the 11 calibration fits was found to be 1.3 for $N=11$ degrees of freedom in most cases. The linearity was found to be quite good. The values found for the quadratic coefficient a_2 in the various Pb spectra ranged in absolute magnitude from near zero to 0.2×10^{-6} keV/channel², corresponding to no more than a 3.2-keV quadratic correction at channel 4000.

D. Errors in Energy Calibration

One source of systematic error in the energy calibration is the use of the quadratic to convert channels to energy. The average χ^2 per degree of freedom, 1.3, for the 11 summed low-gain spectra is somewhat larger than the expected $\chi^2/N=1$. Other mathematical forms were tried, such as a cubic, but gave no improvement. However, the proximity of the O^{16*} line to the K lines and of the Na²⁴ or Th C'' lines to the L lines of Pb tends to reduce a possible error due to the use of the quadratic.

To minimize a possible systematic error, the source peaks were fitted in the same way as the x-ray lines using the same shape parameters. That is, the water line was fitted with the same shape parameters as that of the K lines of Pb²⁰⁶, while the Na²⁴ and Th C'' lines were analyzed with the same shape parameters as 'the

TABLE IX. Measured K and L transitions and splittings in Pb isotopes.

Line or splitting	Pb ²⁰⁶	Pb ²⁰⁷	Pb ²⁰⁸
$2p_{3/2}-1s_{1/2}$	5973.98 ± 0.44	5969.68 ± 0.45	5963.77 ± 0.45
$2p_{1/2}-1s_{1/2}$	5788.33 ± 0.48	5784.74 ± 0.49	5778.93 ± 0.50
$3d_{3/2}-2p_{1/2}$	2643.75 ± 0.36	2642.25 ± 0.40	2641.48 ± 0.42
$3d_{5/2}-2p_{3/2}$	2501.45 ± 0.43	2500.86 ± 0.44	2500.07 ± 0.45
$3d_{3/2}-2p_{3/2}$	2458.10 ± 0.38	2457.31 ± 0.44	2456.64 ± 0.47
Δp ($K\alpha$ splitting)	185.65 ± 0.12	184.94 ± 0.19	184.84 ± 0.22
$\Delta p-\Delta d$ ($L\alpha$ splitting)	142.30 ± 0.24	141.39 ± 0.32	141.41 ± 0.35

TABLE X. Calculated energy levels and radiative corrections in Pb²⁰⁶.

Level	Point nucleus (keV)	Perturbation calculation (keV)	Exact ^a calculation (keV)	Vacuum polar. (keV)	Lamb shift (keV)	Anom. mag. dipole (keV)	Total energy (keV)
1s _{1/2}	20 991.435	-4388.913	10 534.108	67.147	-2.302	-0.445	10 598.507
2s _{1/2}	5 385.168	1928.630	3 581.303	19.338	-0.625	-0.072	3 599.945
2p _{1/2}	5 385.168	4148.233	4 785.043	32.343	-0.590	0.238	4 817.034
2p _{3/2}	4 837.053	4501.412	4 602.422	29.806	-0.448	-0.203	4 631.576
3s _{1/2}	2 329.829	1332.018	1 757.281	7.540	-0.257	-0.023	1 764.541
3p _{1/2}	2 329.829	1923.634	2 129.299	10.790	-0.243	0.057	2 139.902
3p _{3/2}	2 166.440	2046.074	2 082.304	10.260	-0.196	-0.058	2 092.310
3d _{3/2}	2 166.440	2161.783	2 162.429	10.514	-0.018	0.062	2 172.987
3d _{5/2}	2 121.883	2120.179	2 120.317	9.860	-0.010	-0.040	2 130.127
4s _{1/2}	1 284.553	873.935	1 036.580	3.577	-0.131	-0.010	1 040.015
4p _{1/2}	1 284.553	1111.043	1 197.458	4.742	-0.122	0.022	1 202.100
4p _{3/2}	1 216.268	1162.743	1 178.646	4.560	-0.100	-0.024	1 183.082
4d _{3/2}	1 216.268	1213.467	1 213.853	4.582	-0.012	0.025	1 218.448
4d _{5/2}	1 197.327	1196.282	1 196.366	4.336	-0.007	-0.017	1 200.678
4f _{5/2}	1 197.327	1197.317	1 197.318 ^b	3.802	-0.000	0.012	1 201.132
4f _{7/2}	1 188.253	1188.250	1 188.250 ^b	3.695	-0.000	-0.009	1 191.937
5s _{1/2}	810.685	604.283	681.573	1.884	-0.075	-0.005	683.377
5p _{1/2}	810.685	722.049	765.406	2.437	-0.069	0.011	767.784
5p _{3/2}	776.055	748.116	756.095	2.355	-0.058	-0.012	758.380
5d _{3/2}	776.055	774.416	774.442	2.347	-0.008	0.013	776.794
5d _{5/2}	766.349	765.731	765.679	2.231	-0.005	-0.009	767.897
5f _{5/2}	766.349	766.340	766.341 ^b	1.947	-0.000	0.006	768.294
5f _{7/2}	761.683	761.680	761.680 ^b	1.895	-0.000	-0.005	763.571
5g _{7/2}	761.683	761.683	761.683 ^b	1.637	-0.000	0.004	763.324
5g _{9/2}	758.931	758.931	758.931 ^b	1.613	-0.000	-0.003	760.541
6s _{1/2}	557.303	435.425	480.316	1.201	-0.047	-0.003	481.466
6p _{1/2}	557.303	505.025	529.662	1.463	-0.044	0.006	531.088
6p _{3/2}	537.422	520.340	524.562	1.440	-0.037	-0.007	525.958
6d _{3/2}	537.422	536.382	536.429 ^b	1.416	-0.006	0.008	537.846
6d _{5/2}	531.810	531.413	531.431 ^b	1.350	-0.003	-0.005	532.773
6f _{5/2}	531.810	531.804	531.804 ^b	1.122	-0.000	0.004	532.930
6f _{7/2}	529.106	529.104	529.104 ^b	1.097	-0.000	-0.003	530.198
6g _{7/2}	529.106	529.106	529.106 ^b	0.920	-0.000	0.002	530.028
6g _{9/2}	527.509	527.509	527.509 ^b	0.907	-0.000	-0.002	528.415
6h _{9/2}	527.509	527.509	527.509 ^b	0.781	-0.000	0.001	528.292
6h _{11/2}	526.454	526.454	526.454 ^b	0.775	-0.000	-0.001	527.227

^a Muon rest mass $m_\mu = 206.767 m_e$, and nuclear parameters $r_0 = 1.19876$ fm, $n = 14.37$.^b Weighted average used.

L lines. This neglects the small variations of the shape parameters over the energy interval between source and x-ray line. However, in all cases the top of the fitted peak was used instead of the center of the fitted Gaussian to establish the location of the line. This procedure is rather insensitive to the values taken for the parameters of the line shape.

An effort was made to minimize shifts in the source peaks due to instrumental effects. The source signals were brought into the apparatus under conditions that simulated the x-ray signal to reduce the possibility of a shift due to rate effects or timing. A shift of 0.2 keV (comparable with the quoted error for x rays in that region) was noted between the 511 γ ray in the source spectrum (whose primary origin was the water source), and the 511-keV peak that appears in all the Pb

spectra (whose origin is pair production by the muonic x rays). The 511-keV peak is a very strong and narrow peak that tests our fitting procedure quite severely. The χ^2 measures of the fits to these peaks were, in fact, somewhat worse than the others, an indication that our assumed line shape is not quite correct. In the end, we used the 511-keV peaks that appeared in the x-ray spectra in the calibrations. Several other checks showed that the shift between source and x-ray peaks was negligible. During the simultaneous running of the Th and Pb²⁰⁶ targets, the 2614-keV γ ray of ThC'' was present in sufficient strength to appear, by accidental coincidence, in the prompt spectra. It was even stronger in the delayed spectra. We also collected it in the source spectra. Analysis of the peak in the delayed and in the source spectra showed no measurable shift between the

TABLE XI. Preliminary analysis of Pb²⁰⁶.

Transition or <i>f</i> s splitting	$E_{\text{expt}} \pm \delta E$ (keV)	E_{calc}^a (keV)	$(E_{\text{expt}} - E_{\text{calc}}/\delta E)^2$	Sensitivity		
				$(\partial E/\partial r_0)_n$ (keV/fm)	$(\partial E/\partial n)_{r_0}$ (keV)	
Energies fitted ^b						
1	$2p_{1/2} - 1s_{1/2}$	5788.33 ± 0.48	5788.06	0.3	-3942	-6.94
2	$3d_{5/2} - 2p_{3/2}$	2501.45 ± 0.43	2500.66	3.4	-450	+0.50
3	$4f_{5/2} - 3d_{5/2}$	971.74 ± 0.20	971.81	0.1	-13	+0.04
4	Δp	185.65 ± 0.12	185.68	0.1	-201	-0.23
5	$\Delta p - \Delta d$	142.30 ± 0.24	142.83	4.9	-195	-0.20
6	Δd	43.47 ± 0.44	42.84	2.1	-5.0	-0.00
7	$\Delta d - \Delta f$	33.98 ± 0.10	33.65	10.9	-5.8	-0.03
Energies not fitted						
8	$3p_{3/2} - 2s_{1/2}$	1507.93 ± 0.80	1510.02	6.8	-725	-1.55
9	$2s_{1/2} - 2p_{1/2}$	1217.81 ± 0.80	1214.29	19.4	+225	+1.70
10	$5g_{7/2} - 4f_{5/2}$	437.86 ± 0.15	437.81	0.11		
11	$\Delta f - \Delta g$	6.61 ± 0.20	6.42	0.90		
	Number of parameters		2			
	N = Number of degrees of freedom		5			
	χ^2/N		4.3			
	r_0 (fm)		1.1997 ± 0.0012			
	n		12.84 ± 0.70			
	c (fm)		6.637 ± 0.038 (6.625 ± 0.01) ^c			
	t (fm)		2.27 ± 0.11 (2.31) ^c			

^a Muon rest mass $m_\mu = 206.767m_e$.^b The fit was made using ±0.12 keV as error for $\Delta p - \Delta d$.^c Reference 8.

two. Also, certain La- and Y-capture γ rays which were strong enough to appear with good intensity in the prompt as well as in the delayed spectra, showed no shift between the two spectra. Thus, there was no systematic shift between the prompt, delayed, and source peaks, except for the small shift in the 511-keV peaks mentioned above.

There were also no evident systematic shifts due to rate effects (different beam rates, different source rates, etc.). A check on one type of rate effect was made using the runs with the Th²³² target. As mentioned above, this target is also a strong source of γ rays and produces a much higher rate in the Ge detector than when other targets are used, but no effect on the energy determinations due to its presence could be detected.

A possible systematic shift in the energy due to Compton scattering in the targets was checked by the observation that there was no shift in the muonic x-ray lines from natural-Pb targets of greatly different thicknesses measured simultaneously in the two target positions.

Finally, there was agreement within the quoted errors, between the high- and low-gain energy measurements of the $4f-3d$ and $5g-4f$ transitions. These transitions were measured under different gain settings of the electronics and with different sources providing the absolute energy calibrations. In the case of the $6h-5g$ transition, there was a difference in energy of about

1 keV between the high- and low-gain results. But this could be accounted for because in the low-gain data, the $6h-5g$ transition appears in a part of the ADC where the nonlinearity was too large to be removed completely by our procedure. The quoted values for the $6h-5g$ transition are from the high-gain results.

In carrying out the runs at the high-gain setting, a number of independent changes were introduced. A new set of calibration sources and different electronic settings changed a number of the factors, such as the rates in the analysis system and the number of channels in a peak. Also, natural-Pb targets of different thicknesses were used. Thus, the accuracy of the data and the method of analysis were checked under quite different conditions and found to give consistent results.

E. Pb X-Ray Energies

The nine Pb²⁰⁶ summed spectra were all separately calibrated in energy using the quadratic dependence, Eq. (7). The errors in the energies were obtained by propagating the errors of the $E-C$ coefficients, using the appropriate correlation coefficients, and folding in the statistical errors in the peak positions. The final energies were obtained by taking a weighted average over all of the summed spectra. The results for the principal transitions in Pb²⁰⁶ are presented in Table VII. For Pb²⁰⁶, Table VII includes, for comparison, some

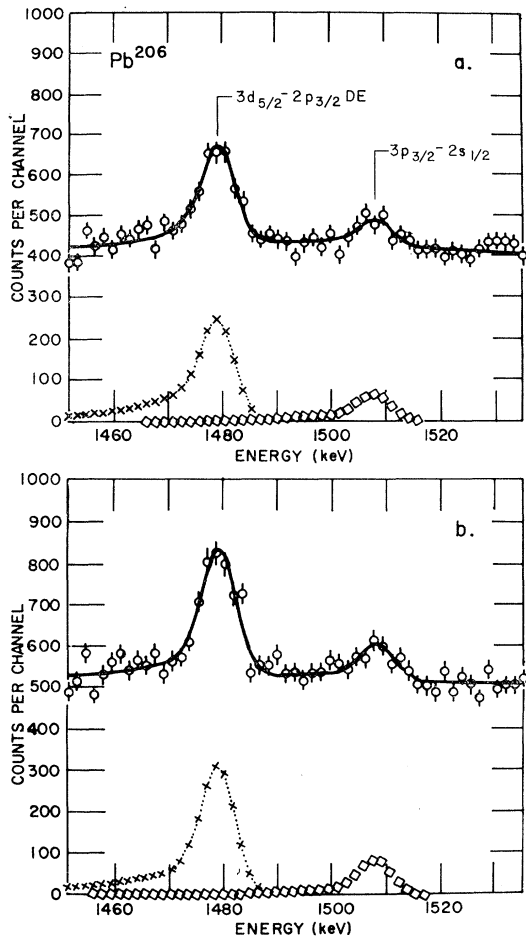


FIG. 13. Fitting of the $3d_{5/2}-2p_{3/2}$ DE and the $3p_{3/2}-2s_{1/2}$ peaks. (a) and (b) refer to two different sets of data.

measurements from recently published work.^{3,8,9} In general, the agreement is well within the quoted errors. The worst discrepancy is with our own earlier measurement of the $K\alpha$ -line splitting Δp , which was too high by 1.4 times the previously quoted error. The values listed for the first four lines in Table VII derive from a weighted average of 27 measurements, 3 from each of 9 summed spectra. In the case of the weak $3d_{3/2}-2p_{3/2}$ transition and the splitting Δd that involves this line, only the FE peak was strong enough to be analyzed properly. Thus, the value of Δd was obtained by averaging the nine differences, $E(3d_{5/2}-2p_{3/2}) - E(3d_{3/2}-2p_{3/2})$ from the nine summed spectra. The value of $E(3d_{3/2}-2p_{3/2})$ listed in Table VII, however, was obtained by subtracting Δp from the value $E(3d_{3/2}-2p_{1/2})$. This is more accurate than the value which is obtained by subtracting Δd from $E(3d_{5/2}-2p_{3/2})$, and differs slightly from it. For the lines of lower energy, only the FE peak is available, so that only one measurement

⁸ H. L. Acker, G. Backenstoss, C. Daum, J. C. Sens, and S. A. deWit, Nucl. Phys. 87, 1 (1966).

⁹ R. J. Powers, Phys. Rev. 169, 1 (1968).

per summed peak was used in the averaging. In some cases, where it was clear that the isotope shift was negligible, the data from Pb^{207} , Pb^{208} , and from the natural-Pb sample were included in the average.

To obtain a realistic estimate of the errors, we investigated the dispersion of the individual measurements. The χ^2 per degree of freedom turned out to be 1.8, 1.4, and 1.9 for the $2p_{1/2}-1s_{1/2}$, $3d_{3/2}-2p_{1/2}$, and $3d_{5/2}-2p_{3/2}$ transitions, respectively. The fine-structure splittings had a specific χ^2 of 1.3 for $2p_{3/2}-2p_{1/2}$ and 1.6 for $3d_{3/2}-3d_{5/2}$. We also constructed ideograms to show the distribution of the measurements. In the case of the transition energies, these showed a long tail on the low-energy side, due presumably to systematic effects in the calibration. The ideograms for the fine-structure separations were more symmetric and more nearly normally distributed. Systematic effects tend to cancel in this case which involves the measurement of a small energy difference. To take into account these deviations from normal behavior, we increased the calculated error by a factor of 4 for the transition energies, and by a

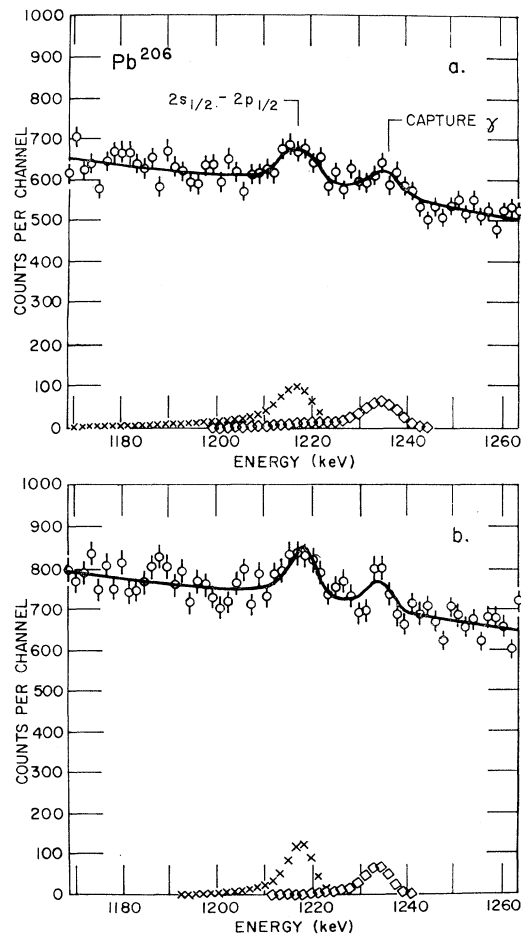


FIG. 14. Fitting of the $2s_{1/2}-2p_{1/2}$ transition. The higher line is a capture γ ray. (a) and (b) refer to two different sets of data.

TABLE XII. Final analysis of Pb²⁰⁶ data.

No.	Transition or <i>fs</i> splitting	E_{expt} (keV)	δE (keV)	ΔE (keV)	E_{calc}^a (keV)	E'_{calc}^a (keV)
1	$3d_{3/2}-2p_{1/2}$	2643.75	0.36	0.47	2644.56	2644.07
2	Δp	185.65	0.12	0.15	185.70	185.46
3	$\Delta p-\Delta d$	142.30	0.24	0.25	142.83	142.60
4	$3p_{3/2}-2s_{1/2}$	1507.93	0.80	0.82	1508.90	1507.64
5	$2s_{1/2}-2p_{1/2}$	1217.81	0.80	0.82	1216.24	1217.11
6	$2p_{1/2}-1s_{1/2}$	5788.33	0.48	0.93	5787.12	5781.54
7	$4f_{5/2}-3d_{3/2}$	971.74	0.20		971.86	971.85
8	Δd	43.47	0.44		42.87	42.86
9	$\Delta d-\Delta f$	33.98	0.10		33.68	33.67
	Energies fitted				1-6	1-5
	Number of parameters				2	2
	N = number of degrees of freedom				4	3
	χ^2/N				3.59	1.42
	r_0 (fm)				1.1979 ± 0.0009	1.1987 ± 0.0006
	n				13.99 ± 0.56	14.37 ± 0.41
	$\Delta(n, r_0)^b$				0.892	0.578
	c (fm)				6.692 ± 0.025	6.715 ± 0.019
	t (fm)				2.102 ± 0.079	2.053 ± 0.055

^a Muon rest mass $m_\mu = 206.767 m_e = 105.659$ MeV.^b Reference 35.

factor of 2 for the splittings. The errors quoted in Tables VII-IX were obtained using this prescription.

In some cases an uncertainty in the background subtraction introduces an additional uncertainty in the value of the energy. This can be caused by the presence of a Compton edge near or under a peak. The error in $\Delta p-\Delta d$ was increased by an additional factor of 2 for this reason.

In the case of some higher transitions, the presence of other weaker lines of nearly the same energy may make a precise energy determination difficult. For example, there are 13 transitions of the type 6-5 lying within 3 keV of the principal transitions $6h_{9/2}-5g_{7/2}$ and $6h_{11/2}-5g_{9/2}$. Since these lines appear unresolved in our data and since the relative intensities are uncertain, we are able to give only a measure of the center of gravity of the group. Lines in this category and weak transitions are discussed in more detail below.

One check on the internal consistency of our method is to calculate the energy of the source peaks by using the $E-C$ coefficients and averaging the results in the same way as for the Pb²⁰⁶ x rays. This was done for the 11 summed spectra in the low-gain series, with the results given in Table III. Another check is provided by the measurement of those x-ray lines which can be calculated without significant corrections from finite nuclear size and radiative effects. Again the agreement was consistent with the stated errors (see Table XX below).

F. 2s Transitions

A particular interest is associated with transitions involving the 2s level. These transitions are quite weak

and have not previously been reported for the heavy elements. They are important because of their unique sensitivity to the shape of the nuclear charge distribution.

Since we had accumulated a large amount of data for Pb²⁰⁶, we were able to identify and measure two transitions involving the 2s level. For this purpose almost all the Pb²⁰⁶ data were divided into two approximately equal groups which were summed channel by channel. The transition $3p_{3/2}-2s_{1/2}$, which lies close to $3d_{5/2}-2p_{3/2}$ (DE), is shown in Fig. 13(a) for group-I data and in Fig. 13(b) for group-II data. Having a well-known line nearby simplifies the energy determination. For each group of data, the two lines were fitted simultaneously with the result shown in the figure. The energy of the $3p_{3/2}-2s_{1/2}$ line was obtained by difference from the established value for $3d_{5/2}-2p_{3/2}$ (DE).

A line appears in the X and $X\bar{A}$ (prompt) spectra of Pb²⁰⁶ which, because of its energy and intensity, we have identified as the $2s_{1/2}-2p_{1/2}$ transition. This assignment is open to some question because there is a capture γ ray which appears in the $\Gamma\bar{A}$ (delayed) spectrum at the same energy, within errors. However, the contribution of this capture γ ray to the prompt line can be calculated from a knowledge of the width of the time windows which define the $\Gamma\bar{A}$ and the $X\bar{A}$ count. The situation is complicated by losses in the $X\bar{A}$ count due to anticoincidence pulses from the x-ray cascade. It turns out, however, that less than half of the intensity of the prompt peak can be accounted for in this way. It was somewhat disconcerting to find that the companion line $2s_{1/2}-2p_{3/2}$, which should appear with about the same intensity 185.6 keV below, is not there. The

TABLE XIII. Interpretation of isotope shifts.

Quantity	207-206		208-206	
	IS _{expt} (keV)	IS _{calc} (keV)	IS _{expt} (keV)	IS _{calc} (keV)
$2p_{3/2}-1s_{1/2}$	4.30 ± 0.10	4.10	10.21 ± 0.10	10.19
$2p_{1/2}-1s_{1/2}$	3.59 ± 0.10	3.86	9.40 ± 0.15	9.67
$3d_{3/2}-2p_{1/2}$	1.50 ± 0.18	1.05	2.27 ± 0.22	2.04
$3d_{5/2}-2p_{3/2}$	0.59 ± 0.11	0.81	1.38 ± 0.14	1.53
Δn	-0.37 ± 0.30		-0.42 ± 0.17	
Δr_0 (fm)	-0.00044 ± 0.00042		-0.00083 ± 0.00024	
Δc (fm)	-0.010 ± 0.013		-0.0035 ± 0.0074	
Δt (fm)	$+0.051 \pm 0.042$		$+0.061 \pm 0.024$	
χ^2/N	10.8		2.95	
$\Delta(\Delta n, \Delta r_0)^a$	0.299		0.169	

^a Reference 35.

$2s_{1/2}-2p_{1/2}$ line as seen in the $X\bar{A}$ spectrum together with its fit, is shown in Fig. 14. A higher line is present but this appears also in the delayed spectrum. In this case, all the intensity found in the prompt peak is due to the capture γ ray. Curiously enough, the energy of this line is within 0.6 keV of that expected for the transition $6p_{1/2}-3s_{1/2}$. However, the expected intensity of this x ray is well below the sensitivity of the present experiment. The measured energies are included in Tables XI and XII below.

V. MEASUREMENT OF ISOTOPE SHIFTS

The spectra of the separated Pb isotopes were analyzed to determine directly the (206-207), and (206-208) isotope shifts (IS), in both the K and L lines. IS's in the $4f-3d$ and higher lines were too small to be measured, although an analysis was attempted. A set of 10 runs in which the three separated isotopes occupied the two target positions in rotation were used for the determination of the isotope shift. This resulted in 20 spectra which were combined by simple summing to give three summed spectra, one for each isotope with equal exposure in the two target positions.

Fitting of the principal transitions was done by using the same shape parameters, listed in Table I, for each of the three isotopes, to determine the position and amplitude parameters C_0 and N_0 . Because the line-shape parameters were kept the same, the three isotope shifts were obtained simply by taking the difference between the values of C_0 found for each isotope, multiplied by 1.6 keV/channel to give the result in keV. Since the 206 and 207 targets had some amount of the other isotopes present, each of their peaks was fitted by combining three peaks, one for each isotope, keeping the amplitudes proportional to the isotopic abundance as given in Table II. The three peaks of the same transition were fitted simultaneously, with the constraint that the channel position of the same isotopic com-

ponent in all three targets be kept the same. The isotope contamination in the Pb^{208} target was so small that it was ignored.

For the K lines, the isotope shift was determined for the DE, SE, and FE peaks, and the results averaged. For the L lines, only the FE peaks were analyzed, since the DE and SE peaks had relatively poor statistics. The results are summarized in Table VIII.

As a check, we used a different fitting procedure, avoiding the use of a particular functional form for the peak shape. The shift between two peaks was obtained after background subtraction and normalization, by incrementing the channel positions of the one peak with respect to the other until the overlap as measured by a χ^2 criterion was a maximum. Shifts obtained this way agreed with those obtained by our standard method within the quoted accuracies.

The measurements reported by Powers⁹ are given for comparison. The agreement is generally good except in the case of the $2p_{3/2}-1s_{1/2}$ transitions, where there is a large but not intolerable discrepancy. Columns 4-7 of Table VIII are discussed in Sec. VI.

Table IX gives the energies of the K and L lines of Pb^{207} and Pb^{208} obtained by adding the isotope shifts to the absolute energies and splittings of Pb^{206} . For the M and higher lines, the isotope shift is so small that the values of the energies for all the Pb isotopes are indistinguishable.

VI. NUCLEAR CHARGE DISTRIBUTION

It is well known that the density of nucleons in nuclei is a constant to a good approximation. This property finds its simplest expression in a model of the nucleus whose charge density is uniform out to a radius R_u given by

$$R_u = r_0' A^{1/3}, \quad (8)$$

where A is the nuclear-mass number and $r_0' \approx 1.2 \times 10^{-13}$ cm over a wide range of A .

For a more precise description of a spherically symmetric nucleus, it has been customary to take the charge distribution to be of the Fermi type

$$\rho(r) = \rho_0 \{ 1 + \exp[n(r/c - 1)] \}^{-1}, \quad (9)$$

with normalization for a nucleus of charge Z ,

$$\rho_0 = (3Z/4\pi c^3) (1 + \pi^2/n^2)^{-1}, \quad (10)$$

where n and c are the parameters which determine the shape and size of the distribution, respectively. This is a simple two-parameter form which approaches the uniform distribution asymptotically with $c \rightarrow R_u$ as $n \rightarrow \infty$.

Some authors prefer to write the Fermi distribution in terms of the skin thickness t , i.e., the distance in which the density falls from 90 to 10% of its central value. This is related to n and c by the relation

$$t = (4c/n) \ln 3. \quad (11)$$

TABLE XIV. Parameters for isotope shifts in Pb.

Parameter	206	207	208
n	14.37	14.00	13.95
r_0 (fm)	1.1987	1.1983	1.1979
c (fm)	6.715	6.706	6.712
t (fm)	2.053	2.105	2.114

It is also conventional to establish a connection with the uniform distribution. The equivalent radius R_{eq} of a charge distribution is that radius of a uniform distribution having the same $\langle r^2 \rangle$. This may be written

$$R_{eq} = [(5/3) \langle r^2 \rangle]^{1/2}, \quad (12)$$

and serves to characterize the distribution in a model-independent way, in terms of its second moment.

The reduced radius appearing in Eq. (8) may now be defined more generally by writing

$$r_0 = [(5/3) \langle r^2 \rangle]^{1/2} A^{-1/3}. \quad (13)$$

Muonic x-ray energies are particularly sensitive to r_0 . This has dictated our choice of r_0 and n as the parameters which are varied in fitting the data.

A further refinement is to introduce a third parameter w capable of varying the central density. The Fermi-type distribution with a parabolic depression is written

$$\rho(r) = \rho_0 (1 + wr^2/c^2) [1 + \exp(n(r-c)/c)]^{-1}. \quad (14)$$

A. Energy Levels

In general, we have in this work used the charge distribution (9) in the Dirac equation to determine the energy levels of the μ -atomic system. For Pb, we have confined ourselves to a spherically symmetric charge

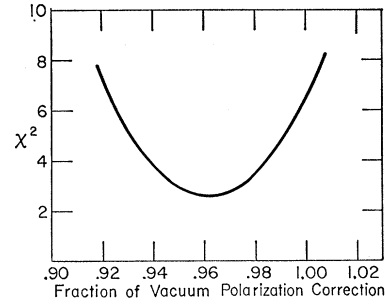


FIG. 15. χ^2 as a function of the assumed vacuum-polarization correction.

distribution and solve the pair of radial equations¹⁰

$$\begin{aligned} df(r)/dr &= \kappa f(r)/r - [E - \mu c^2 - \phi(r)]g(r)/\hbar c, \\ dg(r)/dr &= -\kappa g(r)/r + [E + \mu c^2 - \phi(r)]f(r)/\hbar c \end{aligned} \quad (15)$$

with

$$\phi(r) = -\frac{Ze^2}{r} + \frac{4\pi e^2}{r} \int_r^\infty \rho(r') (r'^2 - rr') dr' \quad (16)$$

and

$$\int_0^\infty (f^2 + g^2) dr = 1. \quad (17)$$

Here f and g are the small and large components of the solution,

$$\kappa = l \quad \text{if } j = l - \frac{1}{2}, \quad \kappa = -l - 1 \quad \text{if } j = l + \frac{1}{2},$$

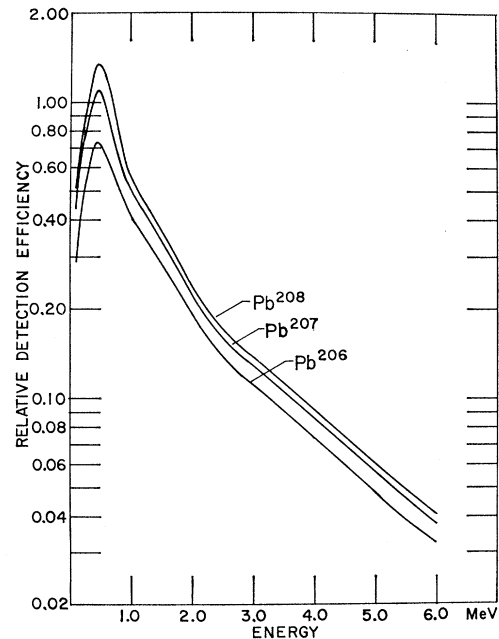


FIG. 16. Relative detection efficiency for the three targets used in this experiment.

¹⁰H. A. Bethe and E. E. Salpeter, *Quantum Mechanics of One and Two Electron Atoms* (Academic Press Inc., New York, 1957), Eqs. (14.12) and (17.1).

TABLE XV. Comparison with Pb²⁰⁸ electron scattering.

Type of meas.	Energy (MeV)	c (fm)	t (fm)	$\langle r^2 \rangle^{1/2}$ (fm)	Ref.
Electron scat.	84, 153, 186	6.5±0.13	2.3±0.23	5.42	43
	53	6.66±0.09	2.21±0.17	5.48±0.07	44 ^a
	175	6.47±0.03	2.30±0.03	5.38±0.03	45
	250	6.48±0.03	2.31±0.02	5.39±0.03	45
Muonic x ray		6.70±0.08	2.15±0.30	5.484±0.014	3
		6.67±0.01	2.21	5.493±0.007	8 ^a
		6.712±0.020	2.114±0.060	5.4978±0.0030 ^b	This work

^a Natural Pb.^b For comparison with natural Pb, the weighted average of our results is 5.4928±0.0030 fm.

with j and l the total and orbital angular momentum of an eigenstate, E the total energy of the muon in the muon-nucleus c.m. system, and μc^2 the reduced mass of the muon. To find the eigenvalues of Eq. (15), we start with the point-nucleus solution for the binding energy W_{nk} which is available in analytic form¹⁰:

$$W_{nk}/(\mu c^2) = 1 - \left[1 + \left(\frac{\alpha Z}{n - |k| + (k^2 - \alpha^2 Z^2)^{1/2}} \right)^2 \right]^{-1/2}, \quad (18)$$

where $\alpha = e^2/\hbar c$ is the fine-structure constant. This corresponds to using the first term in expression (16) for the potential $\phi(r)$, and always overestimates the binding energy. We obtain an underestimate by a perturbation calculation using the point-nucleus wave functions and the second term in (16), calculated by numerical integration. We can come close to the true eigenvalue for the finite nucleus by taking a weighted average of these two estimates. We use the expectation value of the muon radius $\langle r \rangle$ and the nuclear radius R_n as weights for the perturbation value and the point-nucleus value, respectively. This prescription is sufficient to give the higher energy levels quite accurately; for the lower levels it serves as a starting point for a numerical solution of Eq. (15).

For the numerical solution, we use the first Bohr radius a as the matching radius and use 250 mesh points to calculate the inner functions f_i and g_i by numerical integration from 0 to a . For $r > a$, we transform the Dirac equation in terms of a new variable $s = 1/r$, carrying out a numerical integration, again with 250 mesh points between $s = 0$ and $s = 1/a$, to obtain the outer functions f_0 and g_0 , and calculate the quantity

$$D = f_i(a)/g_i(a) - f_0(a)/g_0(a). \quad (19)$$

With D calculated for a set of closely spaced estimates of the eigenvalue, an interpolation program finds the energy value, within 10 eV, that would make $D = 0$.

B. Radiative Corrections

The eigenvalues that come from the numerical solution of the Dirac equation do not describe the energy levels of the muonic atom accurately enough. Several corrections must be taken into account.

The most important correction is the vacuum polarization, which arises from the emission and reabsorption of virtual electron-positron pairs. To order $\alpha = e^2/\hbar c$ and for a general nuclear charge distribution $\rho(r)$, the vacuum polarization may be written as a correction to the electrostatic energy¹¹⁻¹³ $\phi(r) + \phi_p(r)$. Here $\phi_p(r)$ is given by¹⁴

$$\phi_p(r) = \frac{2\alpha e^2}{3r} \lambda_e \int_0^\infty \rho(r') r' \left[\chi_2 \left(\frac{r+r'}{\lambda_e} \right) - \chi_2 \left(\frac{|r-r'|}{\lambda_e} \right) \right] dr', \quad (20)$$

where $\chi_n(\xi)$ is the integral

$$\chi_n(\xi) = \int_1^\infty (1/z^n) (1 + 1/2z^2) (1 - 1/z^2)^{1/2} \exp(-2\xi z) dz, \quad (21)$$

and λ_e is the Compton wavelength of the electron. It is rather unwieldy to use Eq. (20) in actual calculation as it stands. Following Glauber *et al.*¹⁵ who give an expansion for χ_1 , we have expanded χ_2 with the result

$$\chi_2(\xi) = \sum_{k=0}^\infty [a_k(2\xi)^k \exp(-2\xi) + b_k(2\xi)^{2k+1} E_i(2\xi)], \quad (22)$$

where $E_i(2\xi)$ is the exponential integral

$$\int_1^\infty \frac{\exp(-2\xi z)}{z} dz.$$

The first few coefficients have been calculated and are

¹¹ R. Serber, Phys. Rev. **48**, 49 (1935).¹² E. A. Uehling, Phys. Rev. **48**, 55 (1935).¹³ K. W. Ford and J. G. Wills, Nucl. Phys. **35**, 295 (1962).¹⁴ R. C. Barrett, S. J. Brodsky, G. W. Erickson, and M. H. Goldhaber, Phys. Rev. **166**, 1589 (1968).¹⁵ R. Glauber, W. Rarita, and P. Schwed, Phys. Rev. **120**, 609 (1960).

TABLE XVI. Relative intensity corrections for the FE peaks in the Pb isotopes.

Energy (keV)	Rel. det. eff.	Pb ²⁰⁶		Target Pb ²⁰⁷		Pb ²⁰⁸	
		Atten.	Total eff.	Atten.	Total eff.	Atten.	Total eff.
431	2.510	0.290	0.728	0.402	1.009	0.452	1.135
438	2.460	0.296	0.728	0.409	1.006	0.459	1.129
936	0.860	0.519	0.446	0.646	0.555	0.701	0.603
937	0.850	0.521	0.443	0.647	0.550	0.702	0.597
971	0.820	0.530	0.435	0.656	0.538	0.710	0.582
2460	0.215	0.634	0.136	0.757	0.163	0.803	0.173
2500	0.210	0.650	0.137	0.758	0.159	0.804	0.169
2640	0.195	0.653	0.127	0.761	0.148	0.806	0.157
5790	0.055	0.647	0.0356	0.755	0.0415	0.800	0.0440
5970	0.052	0.645	0.0335	0.754	0.0392	0.799	0.0416

listed here:

$$\begin{aligned}
 a_0 &= +0.88358, & a_4 &= -0.00318, \\
 a_1 &= +0.02376, & b_0 &= -1, \\
 a_2 &= -0.00708, & b_1 &= 0, \\
 a_3 &= +0.00331, & b_2 &= 0.00312.
 \end{aligned}$$

Cutting off the expansion at a_4 and b_2 introduces an error no larger than 0.01% for $\xi \leq 1$. Thus, for the muon radial coordinate smaller than the electron Compton wavelength, the expansion, cut off as it is, is almost exact.

The electronic vacuum-polarization correction is obtained in the present work from a first-order perturbation calculation using the numerically derived functions,

$$\Delta E_{vp} = \int_0^\infty \phi_p(r) (f^2 + g^2) dr. \quad (23)$$

The vacuum polarization increases the binding energy of the muon, e.g., by 67.1 keV for the 1s level in Pb. It would have been more accurate to add the vacuum-polarization potential directly to the electrostatic potential $\phi(r)$, before the numerical solution of the Dirac equation. However, the error introduced by the first-order perturbation calculation is never larger than 0.4% of the vacuum-polarization correction, somewhat smaller than the experimental errors of the transition energies.

For the muonic Lamb shift, we use the usual expression to order α in the form of a potential energy

$$\phi_{LS}(r) = \frac{4}{3}(\alpha e^2)\lambda_\mu^2 \left[\ln(mc^2/2\Delta E) + \frac{1}{2}\frac{1}{4} - \frac{1}{5} \right] \rho(r), \quad (24)$$

where λ_μ is the Compton wavelength of the muon and ΔE is a certain average of the excitation energy of the muon defined by the Bethe sum.^{14,16,17} Originally, Eq. (24) was derived to explain the $2p_{1/2}$ - $2s_{1/2}$ splitting in

¹⁶ H. A. Bethe, L. M. Brown, and J. R. Stehn, Phys. Rev. **77**, 370 (1950); J. D. Bjorken and S. D. Drell, *Relativistic Quantum Mechanics* (McGraw-Hill Book Co., New York, 1964), pp. 177-179.

¹⁷ B. Fricke, Z. Physik **218**, 495 (1969).

electronic hydrogen and is meant to be valid provided $Z\alpha \ll 1$. This condition is not satisfied very well for heavy high- Z nuclei. However, for heavy muonic atoms, the saving feature is that because of the finite extension of the nuclear charge, the effective value of Z in the critical region $r \sim \lambda_\mu$ is reduced. In Pb, for example, the radius of the nucleus is 7 fm, the 1s Bohr radius 3 fm, while $\lambda_\mu = 1.9$ fm.

A second problem occurs with the Bethe sum. We follow Barrett *et al.*¹⁴ and use for ΔE the binding energy of the muon for the particular energy level to which the Lamb shift is being applied. These authors estimate that the resulting Lamb shift has a 30% uncertainty, arising principally from ΔE .

We calculate the Lamb shift in first-order perturbation. In the region of Pb, the 1s muonic Lamb shift is typically 3.0 ± 1.0 keV. The Lamb shift decreases the binding energy.

The energy shift due to the muon's anomalous magnetic moment can also be written in the form of a correction to the potential energy. To order α , this is

$$\phi_m(r) = -(i\alpha/4\pi)\lambda_\mu [d\phi(r)/dr] \beta \alpha_r, \quad (25)$$

where $\alpha_r = \mathbf{r} \cdot \boldsymbol{\alpha} / r$ and β , $\boldsymbol{\alpha}$ are the usual 4×4 Dirac matrices. In first-order perturbation, the energy shift is

$$\Delta E_m = -\frac{\alpha}{2\pi} \lambda_\mu \int_0^\infty \frac{d\phi(r)}{dr} f(r) g(r) dr. \quad (26)$$

The anomalous-magnetic-moment correction, as formulated in Eq. (26), also suffers the same uncertainties as the Lamb shift resulting from the assumption of $r \gg \lambda_\mu$. But in the lowest levels, where the uncertainty is greatest, the anomalous-magnetic-moment shift is considerably less than the Lamb shift. It is about 0.4 ± 0.1 keV for the 1s level for nuclei in the vicinity of Pb. The anomalous part also increases the fine-structure splittings. In the vicinity of Pb, the $2p$ fine-structure splitting is increased by about 0.4 keV.

C. Calculated Energies

Table X gives calculated binding energies for muonic Pb²⁰⁶ with nuclear parameters close to the values which

TABLE XVII. Relative intensities of the fine-structure components.

Ratio	Symbol	Pb ²⁰⁶	Pb ²⁰⁷	Pb ²⁰⁸	Calc $a = -0.25$
$I(2p_{3/2}-1s_{1/2})$	R_p	1.81±0.03	1.75±0.04	1.64±0.06	1.87
$I(2p_{1/2}-1s_{1/2})$		(1.72±0.10) ^a	(1.75±0.15) ^a	(1.68±0.18) ^a	
$I(3d_{5/2}-2p_{3/2})$	R_d	1.69±0.07	1.68±0.06	1.61±0.09	1.74
$I(3d_{3/2}-2p_{1/2})$		(1.42±0.22) ^a	(1.56±0.34) ^a		
$I(3d_{5/2}-2p_{3/2})$	$R_{d'}$	8.58±1.0	9.00±1.2	10.8±3.0	10.0
$I(3d_{3/2}-2p_{1/2})$					
$I(4f_{7/2}-3d_{5/2})$	R_f	1.43±0.04	1.41±0.03	1.35±0.05	1.41
$I(4f_{5/2}-3d_{3/2})$					
$I(4f_{7/2}-3d_{5/2})$	$R_{f'}$	18.8±5.0	23.0±7.0	18.5±7.0	21.6
$I(4f_{5/2}-3d_{3/2})$					
$I(5g_{9/2}-4f_{7/2})$	R_g	1.03±0.10	1.04±0.10	1.09±0.10	1.29
$I(5g_{7/2}-4f_{5/2})$					

^a Reference 9.^b Reference 8.

were found here (see Table XII below). We include here all levels up to $n=6$. The radiative corrections are explicitly tabulated for each level as well as the point-nucleus values and the perturbation values. The final value of the binding energy does not include other possible corrections, such as those discussed below. It is interesting that whereas the reduction in the binding energy because of the finite size of the nucleus is more than 10 000 keV for the $1s$ level, the reduction is only 1.5 keV already for the $3d_{5/2}$ level. The vacuum-polarization correction in the case of the $4f_{5/2}-3d_{3/2}$ transition is larger than the finite-size effects, 6.7 compared to 4.0 keV. This circumstance provides an opportunity to check the vacuum-polarization effect experimentally.

D. Vacuum Polarization Effect

We have already noted that the $4f-3d$ transitions are relatively insensitive to the shape parameters but have a vacuum polarization correction which is many times greater than the experimental error. This is also true of the $5g-4f$ transitions. Higher transitions are less useful, first because the vacuum polarization correction is smaller, and second, because the lines are unresolved composites of several transitions which make the energy determination less certain. We were able to check the validity of the vacuum-polarization correction using the lines $4f_{5/2}-3d_{3/2}$, $4f_{7/2}-3d_{5/2}$, $5g_{7/2}-4f_{5/2}$, and $5g_{9/2}-4f_{7/2}$. We compared the observed values as given in Table VII with those calculated from the energy levels given in Table X, but taking a fraction B of the vacuum polarization correction for each energy level involved. The first-order vacuum-polarization corrections were increased by 2.2% to take into account higher-order effects as given by Fricke,¹⁷ and the $4f-3d$ and $5g-4f$ transition energies were decreased by 0.06 and

0.09 keV, respectively, to take into account the effect of electron screening, as given by Barrett, *et al.*¹⁴ We calculated the χ^2 of the fit as a function of B , plotting the result in Fig. 15. In this way, we found a best fit of the data for $B=0.961\pm 0.020$. The higher-order corrections are just at the limit of our present accuracy.

Evidence for a vacuum-polarization effect in muonic atoms was first observed by Koslov, Fitch, and Rainwater.¹⁸ Our result is comparable to that which has been deduced¹⁹ from the precision measurements of the $3d-2p$ transition energy in muonic phosphorus.^{20,21} In that work, the vacuum polarization effect in muon physics was estimated to be correct to $\pm 4\%$. By comparison, the same vacuum-polarization effect in electron physics is verified to $\simeq 1\%$ from the Lamb shift and $\simeq 2\%$ from the electron $g-2$ measurement.²²

E. Nuclear Polarization

Next in importance among other possible corrections are those due to nuclear polarization. These arise from a reduction in the Coulomb repulsion due to the penetration of the nuclear volume by the muon. The nucleus shrinks, and the binding energy of each muonic level increases as a result. Such effects, which depend on the nuclear structure, were first invoked by Breit²³ to

¹⁸ S. Koslov, V. Fitch, and J. Rainwater, Phys. Rev. **95**, 291 (1954).

¹⁹ A. Petermann and Y. Yamaguchi, Phys. Rev. Letters **2**, 359 (1959).

²⁰ J. Lathrop, R. A. Lundy, S. Penman, V. L. Telegdi, R. Winston, and D. D. Yovanovitch, Nuovo Cimento **17**, 114 (1960).

²¹ S. Devons, G. Gidal, L. M. Lederman, and G. Shapiro, Phys. Rev. Letters **5**, 330 (1960).

²² G. Charpak, F. J. M. Farley, R. L. Garwin, T. Muller, J. C. Sens, and A. Zichichi, Nuovo Cimento **37**, 1241 (1965).

²³ G. Breit, G. B. Arfken, and W. W. Clendenin, Phys. Rev. **78**, 390 (1950).

TABLE XVIII. Total intensity ratios in the principal transitions of the Pb isotopes.

Ratio	Symbol	Pb ²⁰⁶	Pb ²⁰⁷	Pb ²⁰⁸	Calc ^a <i>a</i> = -0.25
$I(3d-2p)$	$R_{L/K}$	0.91±0.27 (0.14) ^b	0.98±0.30 (0.15) ^b	0.68±0.20 (0.10) ^b	0.74
$I(2p-1s)$					
$I(4f-3d)$	$R_{M/L}$	0.83±0.25 (0.16) ^b	0.71±0.21 (0.14) ^b	0.84±0.25 (0.16) ^b	0.76
$I(3d-2p)$					
$I(5g-4f)$	$R_{N/M}$	0.70±0.21 (0.11) ^b	0.83±0.25 (0.13) ^b	0.80±0.24 (0.12) ^b	0.74
$I(4f-3d)$					

^a Reference 50.^b Relative error for comparing a given ratio among the isotopes.

explain the anomalous behavior of the isotope shifts seen in the optical spectra of ordinary (electronic) atoms. For muonic atoms, calculations made by many authors²⁴⁻³⁰ have given widely different results depending on the nuclear model used. Recently, Cole³¹ and also Chen,³² using experimental inelastic electron scattering cross sections to make their calculation less model-dependent, have shown that nuclear-polarization effects result in an increase in the muon binding in Pb of about 6 keV for the 1s state and about 2 keV for the 2p state. However, a considerable uncertainty attaches to these calculations ±50% according to Cole and ±30% according to Chen, considerably larger than the experimental error. A report in which we tried to use our determinations to provide a measure of the nuclear-polarization effect has already been published.⁴ We return to this and other effects of nuclear structure below.

F. Other Corrections

Other corrections that have been considered^{14,33,34} have been ignored throughout most of this work. This is not quite correct since the electron screening correction¹⁴ becomes almost significant for the higher transitions. We have taken it into account only for the purposes of checking the vacuum-polarization correction as given above. The nonelectromagnetic (weak) interaction of the muon with the nucleus has been estimated to be of the order of a few eV. The error introduced by using the reduced mass in the Dirac equation has been estimated¹⁴ to be less than 1 keV for the 1s level and negligibly small for levels with $n \geq 2$.

²⁴ L. N. Cooper and E. M. Henley, Phys. Rev. **92**, 801 (1953).²⁵ W. Lakin and W. Kohn, Phys. Rev. **94**, 787 (1954).²⁶ E. Nuding, Z. Naturforsch. **12a**, 187 (1957).²⁷ W. Greiner, Z. Physik **164**, 374 (1961).²⁸ F. Scheck, Z. Physik **172**, 239 (1963).²⁹ W. Pieper and W. Greiner, Phys. Letters **24B**, 377 (1967).³⁰ R. K. Cole, Jr., Phys. Letters **25B**, 178 (1967).³¹ R. K. Cole, Jr., Phys. Rev. **177**, 164 (1969). The shifts extrapolated to Pb were taken to be 5.7, 0.9, 1.8, and 0.1 keV for the 1s, 2s, 2p, and 3d states, respectively. Cole estimates the results to be accurate to a factor of 2.³² Min-Yi Chen, Ph.D. thesis, Princeton University, 1968 (unpublished).³³ D. L. Hill and K. W. Ford, Phys. Rev. **94**, 1617 (1954).³⁴ G. E. Pustovalov, Zh. Eksperim. Teor. Fiz. **32**, 1519 (1957). [English transl.: Soviet Phys.—JETP **5**, 1234 (1957)].

We have ignored the mixing of nuclear and μ -atomic states even though this may have non-negligible effects on the energy levels.

G. Nuclear Parameters

The nuclear parameters for the Fermi charge distribution were derived from the experimental energies in the following manner: A fine rectangular mesh of the parameters r_0 and n (or w , r_0 , and n in the three-parameter fits) was chosen and a set of transition energies and splittings calculated for each point on the mesh. The mesh was chosen to surround approximate values of the parameters obtained by an earlier interpolation within a coarser mesh covering a wider range of the parameters. The final mesh was chosen to be so fine that the interpolation was practically linear.

The interpolations were carried out by a multi-dimensional Lagrangian method. Using the experimental energies and their errors, the parameters were varied in a systematic way until a minimum in χ^2 was obtained.

We first carried out such a fit in a conventional way,³ including the corrections for the radiative effects but making none for the nuclear polarization. We used seven energies; the principal transitions $2p_{1/2}-1s_{1/2}$, $3d_{5/2}-2p_{3/2}$, and $4f_{5/2}-3d_{3/2}$, and the splittings Δp (K lines), $\Delta p-\Delta d$ (L lines), Δd (L lines), and $\Delta d-\Delta f$ (M lines). These energies were fitted with just two parameters, r_0 and n ; w was set equal to zero. The results are given in Table XI. Here we give the values of r_0 and n found from the best fit as well as the corresponding values of c and t to permit a direct comparison with the work of Acker *et al.*⁸ It is seen that there is a good agreement as far as the determination of the nuclear parameters is concerned. This was to be expected in view of the good accord already noted for the experimental energies.

Table XI also gives a comparison of the calculated energies with those measured. The agreement is fairly good, well within 1 keV in every case. Nevertheless, the χ^2 per degree of freedom turned out to be 4.3, a figure too high to be considered a good fit.

The largest discrepancy occurs for the $\Delta d-\Delta f$ splitting. The reason for this is not clear, although the small error assigned does invite a large contribution to χ^2 .

TABLE XIX. Population of μ -atomic states of Pb from a cascade calculation.^a For each doublet the upper number refers to the state with the higher j .

n	$l=0$	$l=1$	$l=2$	$l=3$	$l=4$	$l=5$	$l=6$	$l=7$	$l=8$	$l=9$	$l=10$	$l=11$	$l=12$	$l=13$
14	0.0318 0.0000	0.0496 0.0248	0.0579 0.0386	0.0601 0.0451	0.0585 0.0468	0.0547 0.0456	0.0497 0.0426	0.0442 0.0387	0.0387 0.0344	0.0335 0.0302	0.0287 0.0261	0.0244 0.0224	0.0206 0.0190	0.0173 0.0160
13	0.0002 0.0000	0.0004 0.0003	0.0009 0.0006	0.0016 0.0012	0.0027 0.0022	0.0042 0.0035	0.0058 0.0050	0.0076 0.0067	0.0096 0.0085	0.0116 0.0104	0.0136 0.0124	0.0155 0.0142	0.0173 0.0160	
12	0.0002 0.0000	0.0008 0.0005	0.0011 0.0008	0.0020 0.0015	0.0034 0.0028	0.0053 0.0044	0.0075 0.0065	0.0101 0.0089	0.0130 0.0116	0.0161 0.0145	0.0193 0.0176	0.0226 0.0207		
11	0.0003 0.0000	0.0010 0.0006	0.0014 0.0009	0.0026 0.0019	0.0046 0.0037	0.0072 0.0060	0.0105 0.0090	0.0145 0.0127	0.0191 0.0169	0.0243 0.0218	0.0300 0.0272			
10	0.0007 0.0000	0.0014 0.0008	0.0018 0.0012	0.0035 0.0026	0.0064 0.0051	0.0103 0.0086	0.0155 0.0133	0.0221 0.0193	0.0303 0.0269	0.0404 0.0363				
9	0.0009 0.0000	0.0017 0.0009	0.0024 0.0016	0.0050 0.0037	0.0093 0.0075	0.0157 0.0131	0.0248 0.0213	0.0374 0.0327	0.0550 0.0489					
8	0.0012 0.0000	0.0022 0.0012	0.0035 0.0023	0.0075 0.0056	0.0148 0.0119	0.0266 0.0222	0.0452 0.0388	0.0757 0.0663						
7	0.0010 0.0000	0.0028 0.0014	0.0054 0.0036	0.0125 0.0094	0.0266 0.0213	0.0530 0.0442	0.1049 0.0899							
6	0.0015 0.0000	0.0044 0.0022	0.0092 0.0062	0.0240 0.0180	0.0589 0.0472	0.1456 0.1214								
5	0.0025 0.0000	0.0074 0.0037	0.0189 0.0127	0.0602 0.0453	0.2020 0.1619									
4	0.0045 0.0000	0.0151 0.0076	0.0551 0.0371	0.2791 0.2103										
3	0.0101 0.0000	0.0466 0.0237	0.3828 0.2588											
2	0.0367 0.0000	0.5859 0.3179												
1	1.0000 0.0000													

^a Reference 50. Initial population of $n=14$ level distributed according to $(2l+1)e^{al}$, with $a = -0.25$.

We have no basis for relaxing the error here, but since this energy is quite insensitive to the charge parameters (see columns 6 and 7) it does not play a significant role in their determination. Simply deleting this quantity from the consideration reduces the χ^2 per degree of freedom to 2.6, a value not large enough of itself to cause too much concern. However, a discrepancy which stands out more clearly appears when the energies obtained for $2s_{1/2}-2p_{1/2}$ and $3p_{3/2}-2s_{1/2}$ are compared with those calculated by use of the parameters of Table XI. The values differ by several standard deviations. These are energies which are fairly sensitive to the nuclear parameters. On the other hand, the transitions $5g-4f$, which are rather insensitive to the nuclear parameters, are found to be in good accord with their expected values.

Table XI also shows the energy sensitivity of the parameters. For each energy we give the partial derivatives $(\partial E/\partial r_0)_n$ and $(\partial E/\partial n)_{r_0}$, evaluated at the point of best fit. It is clear that several of the muonic x-ray energies are quite sensitive to the radius parameter r_0 and relatively insensitive to the shape parameter

n . The circular orbits, $4f$ and higher, are essentially insensitive to the nuclear parameters. For such orbits, the point-nucleus values of the energy given there differ very little from the exact calculation. The dominant role of the $2p_{1/2}-1s_{1/2}$ transition energy should be noted. The great sensitivity of both parameters to this energy exercises a strong constraint on the fit. Thus, if the energy of the $1s$ level is incorrectly calculated, the fitting procedure compensates for this by shifting the parameters away from the values required by the less sensitive energies. The $1s$ level is particularly suspect in this regard since all corrections are largest for this level. In particular, the nuclear-polarization effect not yet included in the calculation discussed so far could make a significant difference here.

Such considerations have led us to attempt a fit without the $2p-1s$ transition. For this we used the five remaining energies most sensitive to the nuclear parameters as listed in Table XI. We included the weak transitions $2s_{1/2}-2p_{1/2}$ and $3p_{3/2}-2s_{1/2}$, and we deleted the less sensitive energies $4f_{5/2}-3d_{3/2}$, Δd and $\Delta d-\Delta f$, reserving these for a comparison check. It also seemed more

correct for the purpose of the χ^2 calculation to include in the error some uncertainty in the radiative corrections. Somewhat arbitrarily, we took this to be 1% of the vacuum polarization value and 30% of the Lamb-shift value. These uncertainties were folded in with the experimental error to give the compound errors used in the fit. They are listed as ΔE in column 5 of Table XII.

Applying the fitting procedure to the first five energies of Table XII, we obtained the parameters and calculated energies of column 7 of Table XII. This fit has a χ^2 per degree of freedom which is 1.42, a value notably better than the value 3.59 obtained when the $2p$ - $1s$ transition energy is included in the fit. The results in this case are listed in column 6. There is only a slight difference between the parameters obtained here and those given in Table XI. The lower χ^2 is due mainly to the augmentation of the errors to allow for the uncertainties in calculating the corrections. We consider the value $\chi^2/N=1.42$, obtained by deleting the $2p$ - $1s$ energy, as good a fit as can be expected under the circumstances, since the nuclear polarization corrections in the $2p$ and higher levels have not been included in the calculation.

The fit is determined by varying the parameters n and r_0 . An error matrix expresses the uncertainty with which these quantities are determined. The diagonal elements give the square of the error as listed in Table XII, whereas the off-diagonal elements give the correlation coefficient.³⁵ The complete error matrix is used in evaluating the errors assigned to the quantities t and c , which we derive from n and r_0 .

It is quite striking that we are able to obtain as good a fit as we have with only two parameters in the nuclear charge distribution. We have tried to improve the fit (with the $2p$ - $1s$ energy included) by adding a third parameter, w in Eq. (14). It turned out, however, that the fit was not improved by taking w different from zero. Similarly, we were not able to improve the fit significantly by assuming the existence of a nuclear halo, suggested by Barrett *et al.*¹⁴ An attempt by Ford and Wills³⁶ to obtain a precision fit to our data with "reasonable" static spherically symmetric charge distributions was also unsuccessful. They even tried some four-parameter functions, although they did not exhaustively vary the parameters.

While we cannot exclude the possibility that some charge distribution with a suitable shape might produce a better fit, the search for such a distribution could hardly be made meaningful until a proper account of possible nuclear effects, especially the nuclear polarization, can be given. Corrections for the latter have not been made so far for lack of adequate theoretical foundation.

We consider that the more reliable values of the

³⁵ In the error matrix E of the parameters a_k , the correlation coefficient for a_m, a_n is defined by $\Delta(a_m, a_n) = E_{mn} (E_{mm}E_{nn})^{-1/2}$.
³⁶ K. W. Ford and J. G. Wills, LASL Report No. LA-DC-10393, 1968 (unpublished).

TABLE XX. Energies and intensities of prominent muonic transitions in Pb²⁰⁶.

Transition	E_{calc}^a (keV)	E_{expt} (keV)	Fraction per μ capture	
			I_{calc}	I_{expt}
$2p_{3/2}-1s_{1/2}$	5967.0 ^a	5974.0 \pm 0.4	0.564	0.421
$2p_{1/2}-1s_{1/2}$	5781.5 ^a	5788.3 \pm 0.5	0.302	0.233
$5d_{5/2}-2p_{3/2}$	3863.7	...	0.012	...
$4d_{3/2}-2p_{1/2}$	3598.6	...	0.024	...
$4d_{5/2}-2p_{3/2}$	3430.9	3429.5 \pm 1.4	0.041	0.022
$3d_{3/2}-2p_{1/2}$	2644.1	2643.8 \pm 0.4	0.221	0.206
$3d_{5/2}-2p_{3/2}$	2501.5	2501.5 \pm 0.4	0.383	0.348
$3d_{3/2}-2p_{3/2}$	2458.6	2458.1 \pm 0.4	0.038	0.040
$6f_{7/2}-3d_{5/2}$	1599.9	1598.2 \pm 1.0	0.012	0.006
$3p_{3/2}-2s_{1/2}$	1507.6	1507.9 \pm 0.8	0.008	0.007
$5f_{5/2}-3d_{3/2}$	1404.7	1404.1 \pm 0.4	0.027	0.022
$5f_{7/2}-3d_{5/2}$	1366.6	1366.0 \pm 0.5	0.038	0.024
$2s_{1/2}-2p_{1/2}$	1217.1	1217.8 \pm 0.8	0.016	0.006
$2s_{1/2}-2p_{3/2}$	1031.6	...	0.021	...
$4f_{5/2}-3d_{3/2}$	971.9	971.7 \pm 0.2	0.197	0.197 ^b
$4f_{7/2}-3d_{5/2}$	938.2	937.8 \pm 0.2	0.279	0.282
$4f_{5/2}-3d_{5/2}$	929.0	928.2 \pm 0.5	0.013	0.015
$4d_{5/2}-3p_{3/2}$	891.6	...	0.014	...
$6g_{7/2}-4f_{5/2}$	671.1	670.9 \pm 0.4	0.025	0.018 ^c
$6g_{9/2}-4f_{7/2}$	663.5	663.1 \pm 0.4	0.032	0.023 ^c
$5f_{5/2}-4d_{3/2}$	450.2	...	0.016	...
$5g_{7/2}-4f_{5/2}$	437.8	438.0 \pm 0.1	0.157	0.171
$5f_{7/2}-4d_{5/2}$	437.1			
$5g_{9/2}-4f_{7/2}$	431.40	431.3 \pm 0.1	0.202	0.176

^a Does not include nuclear polarization or higher-order radiative corrections.

^b Normalized to calculated value.

^c Average from high-gain and low-gain runs.

nuclear parameters are those obtained with the $2p$ - $1s$ energy excluded. In a qualitative sense we may say that when the muon occupies the $1s$ level, the nucleus contracts a little. In the absence of a reliable way to calculate this effect, we restrict our analysis to the $n=2$ and higher levels where such effects are much smaller. As can be seen from Table XII, the calculated value of the $2p_{1/2}-1s_{1/2}$ energy is lower by 6.8 ± 2.3 keV than that measured. The error given derives mainly from the uncertainty in the nuclear parameters given in Table XII. We assume, tentatively, that this difference is significant and is due mainly to nuclear polarization.⁴

We have already indicated some doubt about whether we have correctly identified the $2s_{1/2}-2p_{1/2}$ transition. In view of this, we carried out a calculation in which the $2s_{1/2}-2p_{1/2}$ measurement was not included in the fit. This gave a somewhat smaller "polarization" shift in the $2p$ - $1s$ energy, 5.6 ± 2.8 instead of 6.8 ± 2.3 keV, but left the general conclusions the same.

The magnitude of this discrepancy between the calculated and measured value of the $K\alpha$ energy is quite compatible with Cole's³¹ or Chen's³² calculations. Although this agreement is suggestive, the evidence is not strong enough to draw definite conclusions for two reasons. First, the present analysis is based on the use of a Fermi charge distribution and is, therefore, not as

TABLE XXI. Some unresolved lines in Pb²⁰⁶.

Transition	E_{calc} (keV)	E_{expt} (keV)	Fraction per μ capture	
			I_{calc}	I_{expt}
$7g_{7/2}-5f_{5/2}$	379.0		0.007	
$7f_{7/2}-5d_{5/2}$	378.5		0.002	
$7g_{9/2}-5f_{7/2}$	375.3		0.009	
$7h_{9/2}-5g_{7/2}$	375.1		0.021	
$7h_{11/2}-5g_{9/2}$	373.0		0.013	
7-5	375.3	374.3 ± 0.4	0.052	0.059 ^a
$6g_{7/2}-5f_{5/2}$	238.3		0.020	
$6g_{9/2}-5f_{7/2}$	235.2		0.026	
$6h_{9/2}-5g_{7/2}$	235.0		0.119	
$6h_{11/2}-5g_{9/2}$	233.3		0.146	
6-5	234.4	234.6 ± 0.2	0.311	0.361 ^a
$7g_{7/2}-6f_{5/2}$	143.6		0.005	
$7f_{7/2}-6d_{5/2}$	143.4		0.001	
$7g_{9/2}-6f_{7/2}$	141.9		0.006	
$7h_{9/2}-6g_{7/2}$	141.8		0.022	
$7h_{11/2}-6g_{9/2}$	140.9		0.027	
$7i_{11/2}-6h_{9/2}$	140.9		0.089	
$7i_{13/2}-6h_{11/2}$	140.3		0.105	
$7i_{11/2}-6h_{11/2}$	139.8		0.001	
7-6	140.8	142.1 ± 0.9	0.256	0.181 ^a

^a Average from high-gain and low-gain runs.

general as one would like. Second, if nuclear polarization is present to the extent predicted by the theoretical calculations, it should also affect the higher energy levels. Ideally, one would like to fit the whole set of experimental data to calculated energies which include the corrections for nuclear polarization. We tried to do this using values estimated from Cole's calculations.³¹ We increased the calculated binding energies for the various levels as follows: 5.7 keV for 1s, 1.8 keV for 2p, 0.9 keV for 2s, and 0.1 keV for 3d. A small (10%) improvement in χ^2/N resulted. Multiplying all these values by the same constant factor ranging from 0 to 1.7 did not improve matters significantly. As long as the theoretical uncertainties of the polarization corrections are much larger than the experimental errors, such attempts to fit the data are not very meaningful.

H. Isotope Shift

In Table VIII, the observed isotope shift is compared with a standard shift calculated by holding the nuclear parameters n and r_0 constant. This is in accord with the practice followed in the optical³⁷ and electronic x-ray³⁸ work, and corresponds to the $A^{1/3}$ dependence observed for nuclear radii generally. Our values differ somewhat from those given by Powers,⁹ because his standard shifts were calculated while holding the skin thickness t constant. We take all linear dimensions of the standard nucleus, including t , to vary as $A^{1/3}$.

³⁷ A. Stuedel, Z. Physik **133**, 438 (1952); see the review by P. Brix and H. Kopfermann, Rev. Mod. Phys. **30**, 517 (1958).

³⁸ R. B. Chesler and F. Boehm, Phys. Rev. **166**, 1206 (1968).

If a comparison of the observed to the standard shift (Table VIII) is limited to the 2p-1s transitions, it is seen that the ratio is close to 0.50 for the 206-207 shift and to 0.63 for the 206-208 shift. This is in good agreement with the optical³⁷ and the electronic x-ray work,³⁸ as already found.⁹ Moreover, we find, again in accord with previous work,⁹ that the relative isotope shift $IS(206-207)/IS(206-208) = 0.402 \pm 0.005$, is in good agreement with the optical data.

No such general accord appears in the case of the 3d-2p isotope shifts. Here the observed shift follows more nearly the $A^{1/3}$ rule. In the case of the $3d_{3/2}-2p_{1/2}$ transition, $IS(206-207)$ may be even greater than the standard shift. The result of Powers,⁹ with poorer accuracy, is not in disagreement with this anomalous behavior. The average 206-208 shift for the 3d-2p transitions is 0.86, a value notably closer to 1 than the corresponding value 0.63 for the 2p-1s transitions.

The unknown effects of nuclear polarization, and of nuclear structure more generally, make any interpretation of the isotope shifts somewhat questionable, especially insofar as the 2p-1s transitions are involved. Nevertheless, we thought it would be instructive to see what could be said about the change in the parameters under the assumption that what polarization effect there is remains unchanged in going from one isotope to the next. Thus, we asked the question what change in the quantities r_0 and n alone can account for the observed isotope shifts.

The change in the parameters Δr_0 and Δn which best fit our measured isotope shifts were obtained by an interpolation procedure similar to that described above for finding r_0 and n for Pb²⁰⁶. Using the values $n = 14.37$ and $r_0 = 1.1987$ fm found for Pb²⁰⁶, we calculated the isotope shifts in going to the other two isotopes by changing n and r_0 by small amounts in various directions to form a rectangular mesh with Δr_0 and Δn as the mesh points. The best values of Δr_0 and Δn were those found by interpolation to give a minimum in the total squared deviation between the calculated and the observed isotope shifts. Table XIII lists the measured isotope shifts, the fitted values, and the changes in the parameters corresponding to these values. Table XIV lists the resulting values of the nuclear shape parameters for the three Pb isotopes. The absolute errors on the parameters of Pb²⁰⁶ can be found in Table XII, and the relative errors for Pb²⁰⁷ and Pb²⁰⁸ with respect to Pb²⁰⁶ in Table XIII. The correlation coefficient³⁵ from the error matrix of the parameters is given in both cases to show the basis for the calculation of the errors in the parameters c and t which have been derived from r_0 and n .

In the case of $IS(206-208)$, the fit is notably better and somewhat sharper conclusions can be drawn. We find that $\langle r^2 \rangle$ increases in going from 206 to 208 by 0.152 ± 0.012 fm². In terms of an equivalent radius, which reflects the behavior of the radius in the uniform model, we find $\delta R_{\text{eq}}/R_{\text{eq}} = 0.00253 \pm 0.00020$. This is higher but not essentially different from that which

follows from an interpretation of the optical shift based on the uniform model. With this model Bodmer³⁹ has shown that the ratio of the observed to standard shift is given by

$$IS_{\text{exp}}/IS_{\text{calc}} = (3A/\delta N) (\delta R_u/R_u). \quad (27)$$

Thus, from the value listed in Table VIII, we have $\delta R_u/R_u = 0.00194 \pm 0.00022$. Similarly, the recent result of Chesler and Boehm³⁸ using *K* (electronic) x rays, also listed in Table VIII, leads to $\delta R_u/R_u = 0.00181 \pm 0.00026$.

While these results appear to be somewhat lower than ours, we wish to emphasize here the differences in the interpretation. In the work with electronic atoms, whether in the optical or *K* x-ray region, the quantity measured, because of the flatness of the wave function in the region of the nucleus, is sensitive primarily to the second moment of the nuclear charge distribution and, practically speaking, only $\langle r^2 \rangle$ can be determined from such measurements. The situation for muonic atoms is different. Several transitions can be measured and each samples the nuclear charge distribution in a different way.

An interesting study by Ford and Wills⁴⁰ has shown that, rather model independently, different transitions measure different and specific moments $\langle r^k \rangle$ of the charge distribution. In particular, they show that the $2p_{1/2}-1s_{1/2}$ transition, which measures the $k=2$ moment in the limit of low *Z*, measures the $k=0.80$ moment in Pb with *Z*=82. The $3d_{3/2}-2p_{1/2}$ transition, which measures the $k=4$ moment in the low-*Z* limit, measures the $k=2.29$ moment in muonic Pb. In terms of the uniform model, the equivalent radius is defined by

$$R_k = \left[\frac{1}{8} (k+3) \langle r^k \rangle \right]^{1/k}.$$

To the extent that the actual nucleus does not correspond to the uniform model, each transition will give a different value for the equivalent radius. The fact that our measurements do not give the same value of $\delta R_{\text{eq}}/R_{\text{eq}}$ as the optical isotope shifts simply reflects the fact that we sample differently a charge distribution which is, in fact, not uniform.

Our two-parameter Fermi model of the nucleus presents a somewhat different picture of what is going on when two neutrons are added to the Pb²⁰⁶ nucleus. The result of our analysis, given in Table XIII, subject to the errors given there, shows that, if anything, the half-density radius actually decreases and that it is an increase of the skin thickness *t* (by 3%) that accounts for the increase in $\langle r^2 \rangle$. The interpretation given by Powers⁹ that *c* increases in going from 206 to 208 was based on the assumption, which we consider unjustified, that *t* remains constant.

Important reservations attach to our statement; the errors relative to the effect are large, the Fermi

³⁹ A. R. Bodmer, Nucl. Phys. **9**, 371 (1958/59).

⁴⁰ K. W. Ford and J. G. Wills, Los Alamos Scientific Laboratory Report No. LA-DC-10393, 1968 (unpublished).

TABLE XXII. μ -capture γ rays in Pb²⁰⁶.

No.	E_γ (keV)	Fraction per μ capture
1	203.9±0.8	0.18
2	266.4±0.5	0.03
3	279.3±0.6	0.04
4	416.1±0.6	0.06
5	439.2±0.6	0.03
6	536.5±1.1	0.01
7	599.0±0.7	0.02
8	719.9±0.5	0.07
9	764.3±0.5	0.01
10	794.3±0.4	0.02
11	1014.1±0.4	0.01
12	1136.7±0.6	0.01
13	1218.0±0.5	0.01
14	1233.6±0.7	0.01
15	1434.2±1.6	0.01

distribution may have its own inadequacies in describing the nuclear charge, and the results may be affected by nuclear-structure effects. In view of our difficulty with IS(206–207), it may be that improved precision of measurement alone is not enough to improve our understanding of the isotope shift.

It is interesting to ask what the implications of the isotope shift are in terms of the shell model. It seemed natural to extend the earlier study by Perey and Schiffer⁴¹ of isotope shifts to the results obtained here. The charge distribution for Pb was calculated by evaluating the wave function of each proton in a local Woods-Saxon potential well with the parameters noted below.⁴¹ The strength of the well was fixed by requiring that the separation energy of the last proton be equal to the binding energy of the $3s_{1/2}$ single-proton state. This was satisfied with $V_0=59.990$ MeV for Pb²⁰⁶. The difference between Pb²⁰⁶ and Pb²⁰⁸ was calculated by allowing R_0 to vary as $A^{1/3}$, fixing V_0 at the Pb²⁰⁶ value. A surface-peaked term, added to the potential, had roughly the shape of the $3p_{1/2}$ neutron wave functions. This is the orbit that is filled between Pb²⁰⁶ and Pb²⁰⁸, and one could argue that the change in the potential should have this shape. The strength of this term in the potential was adjusted to fit the separation energy in Pb²⁰⁸.

The distribution of the proton charge in this model is, of course, not the Fermi distribution. However, we could judge the validity of this approach by comparing the second and the fourth moment in the two distributions. The shell model gave an increase in going to Pb²⁰⁸ from Pb²⁰⁶ amounting $\Delta \langle r^2 \rangle^{1/2} = 0.012$ fm and $\Delta \langle r^4 \rangle^{1/4} = 0.014$ fm. The corresponding values deduced

⁴¹ F. G. Perey and J. P. Schiffer, Phys. Rev. Letters **17**, 324 (1966). The analysis given here was kindly carried out on our behalf by J. P. Schiffer at the Argonne National Laboratory. He used the following ordinary and spin-orbit parameters in the Woods-Saxon potential: $R_0=1.26 A^{1/3}$ fm, $a_0=0.65$ fm, $R_{so}=1.00 A^{1/3}$ fm, $a_{so}=0.60$ fm, $V_{so}=6.00$ MeV.

from our Fermi distribution (Table XIII) were $\Delta\langle r^2 \rangle^{1/2} = 0.0138 \pm 0.0011$ fm and $\Delta\langle r^4 \rangle^{1/4} = 0.019 \pm 0.003$ fm. The agreement is good enough to warrant closer attention to the use of the shell model as a way to determine the nuclear-charge distribution.

I. Comparison with Electron Scattering

A number of electron elastic scattering measurements have been reported on Pb^{208} and on natural Pb. These have been done using various incident energies. The low-energy electron scattering is mainly sensitive to the rms radius of the nuclear charge distribution.⁴² At higher energies, the cross section becomes sensitive to higher moments of the shape of the charge distribution. A comparison of the electron scattering results⁴³⁻⁴⁵ with the mesonic x-ray results is given in Table XV. For the electron scattering, we list only the analysis in terms of the Fermi two-parameter charge distribution, although in some cases the addition of the parabolic-depression parameter w of Eq. (14) has provided an improved fit.

There is good accord between the muonic x-ray value of $\langle r^2 \rangle^{1/2}$ and the low-energy electron scattering value of this quantity. Thus, the agreement is good where the measurement is rather model-independent. The higher-energy electron scattering data give a somewhat lower value for this quantity, a possible indication that in this case the result is not model-independent. When the three-parameter Fermi distribution, Eq. (14), was used with the 250-MeV data, the value of $\langle r^2 \rangle^{1/2}$ was raised to 5.54 fm. This supports the idea of the model dependence of the high-energy electron scattering analysis. The high-energy electron scattering data yield higher values of t and lower values of c than the muonic x-ray results. These discrepancies have been discussed by Engfer⁴⁶ and by Elton,⁴⁷ who emphasizes this point. We await the outcome of additional work and more detailed analysis by Hofstadter⁴⁸ and his collaborators.

VII. LINE INTENSITIES

A. Principal Transitions

Although our experiment had not been designed explicitly to make accurate measurements of intensity,

we were able to extract the intensity ratios among the more prominent lines of the spectrum from our data, and to compare these with the expectation from a cascade calculation.^{49,50} Intensity measurements were made by determining the area under each peak, after background subtraction, and then making the necessary corrections for target self-absorption and counter efficiencies. In our case, because of the large size of the target, it was necessary to make a correction for the shadowing effect of the NaI annulus and shield that surrounded the detector. The effect of such corrections is not large in comparing close-lying lines such as those in the fine-structure multiplet, but a much larger uncertainty occurs in comparing lines more widely separated in energy. Nevertheless, we did attempt to measure the ratio of the total intensity in the $3d-2p$ transition (L lines) to that of the $2p-1s$ transition (K lines). Such ratios, which we denote by $R_{L/K}$, $R_{M/L}$, and $R_{N/M}$, have a fairly large error associated with them due to the uncertainties in the corrections. However, in a comparison of these ratios from one isotope to the next, a smaller limit of error can be set.

A calibration of the relative counter efficiency was made using Gd^{169} and Ra^{226} point sources placed on the axis of the diode at the position of the center of the target. The values for the relative intensities of the γ rays emitted by the sources were taken from Ewan and Tavendale.¹ They covered the energy range 0.3–2.4 MeV. The efficiency of the counter above 2.4 MeV was found by extrapolating up to 6 MeV parallel to the curve measured for a 25-cm³ detector by Alexander.⁵¹ This was reasonable because the slopes of the two curves were the same for the values up to 2.4 MeV. This procedure left a large uncertainty in the L -to- K -line relative measurement. No attempt was made to measure the variation of counter efficiency with off-axis position.

An average attenuation factor for each target was calculated by dividing the surface of the target into a fine rectangular mesh, evaluating the amount of absorption due to the target and the materials of the annulus along a line of length r connecting each mesh point to the detector. This was weighed by $1/r^2$ to take into account the variation of the solid angle. Several simplifying assumptions were made: The target was assumed to be uniformly illuminated; the shielding was idealized somewhat; and the detector was taken to be a point.

The correction factors were evaluated at each transition energy as shown in Table XVI. This Table refers to the FE peaks. The relative counter efficiency is given in column 2. The attenuation by absorption and shadowing for the Pb^{206} target is given in column 3, while column 4 gives the relative detection efficiency calculated as the product of the first two. For the Pb^{207} and Pb^{208} targets, which were much smaller, the attenua-

⁴² L. R. B. Elton, *Nuclear Sizes* (Oxford University Press, London, 1961).

⁴³ R. Hofstadter, B. Hahn, A. Knudsen, and J. A. McIntyre, *Phys. Rev.* **95**, 512 (1954); R. Hofstadter, *Rev. Mod. Phys.* **28**, 214 (1956).

⁴⁴ G. J. C. Van Niftrik and R. Engfer, *Phys. Letters* **22**, 490 (1966).

⁴⁵ J. B. Bellicard and K. J. Van Oostrum, *Phys. Rev. Letters* **19**, 242 (1967).

⁴⁶ R. Engfer, in *Proceedings of the International Conference on Electromagnetic Sizes of Nuclei* (Carleton University, Ottawa, 1967), p. 184.

⁴⁷ L. R. B. Elton, in *Proceedings of the International Conference on Electromagnetic Sizes of Nuclei* (Carleton University, Ottawa, 1967), p. 267.

⁴⁸ R. Hofstadter, in *Proceedings of the International Conference on Electromagnetic Sizes of Nuclei* (Carleton University, Ottawa, 1967), p. 129.

⁴⁹ Y. Eisenberg and D. Kessler, *Nuovo Cimento* **19**, 1195 (1961).

⁵⁰ V. Srinivasan and M. K. Sundaresan, *Nuovo Cimento* **57B**, 235 (1968); and (private communication).

⁵¹ T. K. Alexander (private communication).

tion factors are different and are listed separately in columns 5 and 7. A plot of the over-all relative detection efficiency for the three targets is given in Fig. 16.

The measured ratios in the fine structure, as corrected, are given in Table XVII. The symbols used below are defined there. We use an unsubscripted notation for the intensity summed over the fine-structure components in defining the ratios of the total intensity in the principal transitions given in Table XVIII.

All ratios refer to FE peaks, with one exception. In the case of R_p , three different measurements are possible in principle since the $2p-1s$ lines appear quite clearly in DE, SE, and FE peaks. In practice, R_p is determined most accurately and most reliably from the DE peaks, and it is only this value that is given in the Table. Compton edges from the 511-keV annihilation radiation occur near and under the SE peaks in a way that makes the background subtraction too uncertain for precise work. The same thing happens, but to a lesser extent, for the FE peaks. In the case of the $3d-2p$ lines, such effects are quite small, and the weight of statistics favors the FE peaks. Here, and for all lines of lower energy, the ratios recorded refer to the FE peaks.

These results are summarized in Table XVII. The errors include, besides the usual statistical uncertainty, some measure of the uncertainty in the background subtraction and in the efficiency and absorption corrections. The uncertainty in the background may arise not only from the presence of Compton edges, but also from close-lying lines of the higher transitions. In the case of R_p for Pb^{206} , nine separate measurements were averaged and the statistical accuracy was better than 1%. In this case, we augmented the error by 50% to take into account the systematic uncertainties. In the case of R_p , the statistical accuracy was 3% but the presence of higher transitions close by such as $5f_{7/2}-4d_{5/2}$, $5d_{5/2}-4f_{5/2}$, and $5f_{5/2}-4d_{5/2}$, all within 2 keV of either line of R_p , led us to increase the error to 10%.

Table XVII includes the measured values of Powers⁹ and the CERN group.⁸ These are given in brackets under the corresponding values of our numbers. It is seen that the values measured by Powers⁹ are in good agreements with ours. The one disagreement is in the value of R_p found by the CERN group⁸ which is different by 3 standard deviations.

Table XVIII lists the ratios of total line intensities (summed over the fine-structure components) for the principal transitions. A 30% error attaches to these ratios, primarily because of the large uncertainty in the efficiency correction over the large energy interval involved. The smaller error given in brackets is intended for a comparison of a given ratio in one isotope with another.

The last column in both Tables XVII and XVIII are intensities obtained from a calculation of the cascade kindly done for us by Srinivasan and Sundaresan.⁵⁰ The intensities were calculated for different values of the initial population in the $n=14$ levels. Following Eisenberg and Kessler,⁴⁹ the distribution was taken to

be dependent on the orbital-angular-momentum quantum number l with an adjustable parameter ra , namely, proportional to $(2l+1) \exp(al)$. Explicit account was taken of the fine-structure components of each level. For the comparison, we chose $a = -0.25$, because this seemed to give a reasonable fit to the intensities observed. The fine-structure ratios are not very sensitive to the value of a , so we judged the fit on the basis of the total intensity ratios. To give some idea of how the levels are populated as a result of the cascade, we reproduce in Table XIX one of the tables obtained by Srinivasan and Sundaresan⁵⁰ for $a = -0.25$. This calculation overlooks losses by radiationless transitions which may occur as a consequence of the interaction of the muon with the nucleus. The model used here, which starts the cascade calculation at $n=14$, is a simplification which overlooks the molecular⁵² nature of our targets. Muons captured initially in high molecular orbits may make direct transitions to states with $n \leq 14$. For such orbits, l is not a good quantum number, so the usual inhibitions on Δl do not apply. For this reason, all captures need not pass through the $n=14$ state, and direct transitions to states with $n \leq 14$ can have some importance.

Despite these defects, there is quite good general agreement if one compares the Pb^{206} data with the cascade calculations. The observed value of R_p is too low by 2 standard deviations and a similar disparity occurs for R_p . Otherwise, the agreement is fairly good. The disparity for R_p is appreciably larger in Pb^{207} and Pb^{208} . Since these ratios are quite insensitive to the model used in the cascade calculation, the discrepancies here must be taken seriously.

Anomalies in the fine-structure ratio have been reported before. The effect is considerably larger in Tl and Bi where it was first reported by Frati and Rainwater.⁵³ They found $R_p = 1.03 \pm 0.09$ for Tl and $R_p = 1.33 \pm 0.09$ for Bi. This work was done with a NaI detector, but the results have not been altered appreciably by the more recent work^{2,8,9,54} with Ge detectors.

Frati and Rainwater⁵³ tried to explain their results as due to a resonance involving an excited state of the nucleus. Such a resonance can come about because the muon can occupy various atomic states with the nucleus either in its ground state or in one of its excited states. Multipole interaction between the muon and the nucleus can produce appreciable mixing if the states are close enough in energy. This recalls the work of Jacobsohn⁵⁵ and of Wilets,⁵⁶ who anticipated the hyperfine structure that would arise from such quadrupole

⁵² S. S. Gershtein, V. I. Petrukhin, L. I. Ponomarev, and Yu. D. Prokoshkin, Ob'edinennyi Institut Yadernykh Issledovaniy, Dubna, P4-3860, 1968 (unpublished).

⁵³ W. Frati and J. Rainwater, Phys. Rev. **128**, 2360 (1962).

⁵⁴ T. T. Bardin, R. C. Barrett, R. C. Cohen, S. Devons, D. Hitlin, E. Macagno, C. Nissim-Sabat, J. Rainwater, K. Runge, and C. S. Wu, Phys. Rev. Letters **16**, 429 (1966).

⁵⁵ B. A. Jacobsohn, Phys. Rev. **96**, 1637 (1954).

⁵⁶ L. Wilets, Kgl. Danske Videnskab. Selskab, Mat.-Fys. Medd. **29**, No. 3 (1954).

couplings in strongly deformed nuclei. Rolnick⁵⁷ tried to provide a quantitative basis for this idea but was unable to find a big enough effect. Subsequently, Hüfner⁵⁸ showed that the separation of the $3d_{5/2}$ and $2p_{1/2}$ muonic levels in Bi accidentally coincides with an excited nuclear level of suitable spin and parity to allow mixing by $E3$ coupling. This reduces the population of the $d_{5/2}$ level, and hence, the $p_{3/2}$ level to which it decays while the nucleus is left in the excited state at the end of the cascade. A suitable nuclear state (with spin $15/2^+$) appears to exist and quantitative calculations seem to be borne out by the experimental observations.

In the case of Pb^{206} , Sundaresan and Srinivasan⁵⁹ have proposed a somewhat different mechanism based on new experimental evidence for a 1^- level in Pb^{208} at 5.969 MeV.⁶⁰⁻⁶³ In this case, the resonance occurs between the $2p_{3/2}$ muon state with the nucleus in its ground state, and the $1s_{1/2}$ muon state with nucleus in its first excited state. In this case, an $E1$ interaction may mix the two states and deplete the $p_{3/2}$ level. Such an explanation serves to explain the low value of R_p . A consequence would be that since the nucleus would be left in the 1^- state, a cascade of prompt nuclear γ rays could be observed.

B. Other Transitions

In addition to those principal transitions which have been discussed so extensively above, a number of other muonic x rays have been identified. These are shown in Figs. 5 and 6. The identification was made primarily on the basis of the energy, and a check was made to see that the intensity was in reasonable accord with the cascade calculation. Lines which also showed up in the $\Gamma\bar{A}$ (delayed) spectrum were identified as capture γ rays and are discussed below. The $X\bar{A}$ spectrum was useful in determining whether the line was a DE or an FE peak. In some cases a line could be more clearly established in the $X\bar{A}$ spectrum than in the X spectrum.

There are about 180 possible allowed transitions up to $n=6$, but most of these are too weak to be seen. The list reduces to 30 if we limit it to those whose intensity exceeds 1% per muon capture. This is just about at the limit of sensitivity of our experiment. Except for three transitions above the 6000-keV limit of our energy range, all transitions whose intensity according to the cascade calculation exceeds 1% per muon capture are listed in Tables XX and XXI. We have been able to

identify all of these except for five which, however, had calculated intensities quite close to our detection limit. The listing also includes the transitions which contribute to the 7-6 and 7-5 lines, which show up strongly in our data (Fig. 6).

Tables XX and XXI list all the x-ray lines which we have identified in Pb^{206} . They include the principal lines which we have already reviewed as well as the lines mentioned here. A much simpler method of analysis was used for the additional lines. The data was systematically scanned by presenting it on a cathode-ray display under PDP-9 computer control. Instead of attempting a fit, the center of the peak was estimated by eye. This could be done to within $\frac{1}{2}$ -1 channel, and gave a result that agreed quite well with that obtained with our elaborate fitting procedure. The intensity was obtained from the number of counts in the peak above a fitted background. The intensity of each line was compared with $I(4f_{5/2}-3d_{3/2})$ after correcting for relative efficiency (Fig. 16). The value of $I(4f_{5/2}-3d_{3/2})$ was taken to be the cascade calculation value, 0.197 per muon capture, in an attempt to put all intensities on an absolute basis. An error of about 30% is to be understood for these values arising mainly from the doubts in estimating the efficiency over the large energy range involved. This applies to the strong lines. The intensity of the weak lines are subject to much larger errors due to the uncertainties of background subtraction.

The general agreement with the cascade calculation is remarkably good in view of the rather sizeable uncertainties in the measurements. We do not pretend that the cascade calculations, carried out here, can be more than a rough guide to what intensities can be expected. It is quite possible to account for the intensities found in the unresolved 6-5, 7-5, and 7-6 transitions by summing the intensities of the contributing lines from the cascade calculation as indicated in Table XXI. It may be that the deficiency in the $2p-1s$ intensity is a real effect due to radiationless transitions. In some recent work,⁶⁴ we were able to show that at least a part of the missing x rays could be accounted for by radiationless transitions associated with neutron emission. The calculated values of the energy were obtained using as parameters in the Fermi distribution $n=14.37$ and $r_0=1.1987$ fm, as found above. The agreement with the observed values with the exceptions already noted is excellent.

VIII. NUCLEAR γ RAYS

A. Capture γ Rays

The lines which appear in the $\Gamma\bar{A}$ (delayed) spectrum are for the most part nuclear γ rays emitted following muon capture by the nucleus (Figs. 7 and 8). The

⁵⁷ W. B. Rolnick, Phys. Rev. **132**, 1110 (1963).

⁵⁸ J. Hüfner, Z. Physik **190**, 81 (1966); Phys. Letters **25B**, 189 (1967).

⁵⁹ M. K. Sundaresan and V. Srinivasan, Phys. Rev. Letters **21**, 1509 (1968).

⁶⁰ R. Ballini, N. Cindro, J. Delaunay, J. P. Fouan, O. Nathan, and J. P. Passerieux, Phys. Letters **26B**, 215 (1968).

⁶¹ J. Bardwick and R. Tickle, Phys. Rev. **161**, 1217 (1967).

⁶² J. G. Cramer, P. Von Brentano, G. W. Phillips, H. Ejiri, S. M. Ferguson, and W. J. Braithwaite, Phys. Rev. Letters **21**, 297 (1968).

⁶³ A. M. Khan and J. W. Knowles, Bull. Am. Phys. Soc. **12**, 538 (1967).

⁶⁴ C. K. Hargrove, E. P. Hincks, G. R. Mason, R. J. McKee, D. Kessler, and S. Ricci, Phys. Rev. Letters **23**, 215 (1969).

spectrum includes some spurious lines which have entered by accidental coincidence. In this category belong the 511-keV line due to positrons annihilating in the target and its neighborhood, the 2614.5-keV ThC'' line from Th when this was used as a calibration source or as a second target, and the 802.5-keV line which is a natural γ ray from our radio Pb target. The $4f$ - $3d$ muonic x-ray doublet appears (highly attenuated) in the $\Gamma\bar{A}$ spectrum, also by accidental coincidence.

Certain discontinuities will be noted in the $\Gamma\bar{A}$ spectrum. These were introduced because of the way we separated prompt from delayed coincidences. The timing of the γ -ray signal was pulse-height dependent, so the position and widths of the windows used to separate the delayed from the prompt coincidences were chosen differently for each interval of 128 channels in pulse height. Thus, below channel 128 (205 keV) the width of the delay window was 45 nsec; it was increased to 62 nsec for the interval 128–256 channels (205–410 keV), and again to 75 nsec for the interval 256–384 channels (410–614 keV), etc. This showed up as an abrupt change in the background level at these energies.

Quite a bit of structure is evident in the delayed spectrum of Fig. 8. We made an attempt to identify the more prominent γ -ray peaks. Table XXII lists 15 of them. There were some bumps which we felt were too complicated in structure to analyze. Some peaks which we did analyze have unresolved components which we simply disregarded. Our purpose here was simply to make a start in the study of these capture γ rays. In each case we checked to see that the peak appeared in the $X\bar{A}$ spectrum with the intensity expected from the width of the window used to define a prompt coincidence.

We attempted to express the intensity of each γ ray in terms of a fraction per muon capture. For this we made the corrections for decay from the known windows defining the delayed events, using 71.5 nsec as the mean life⁶⁵ of muonic radio-Pb, added a correction for the relative detection efficiency (Fig. 16) and compared the result with the intensity found for the $4f_{5/2}$ - $3d_{3/2}$ muonic x ray. We used the cascade calculation value of 0.197 as the fraction of muonic x rays in this transition per muon capture to express the γ intensity on a per-muon-capture basis.

A large error attaches to our estimate of the intensity, primarily because of the uncertainty in the background subtraction, but also because of our uncertainty in making the decay and efficiency corrections and lack of knowledge of the branching ratio of the x-ray comparison line. We show many lines in which the branching ratio of 1 or 2% may be off by a factor of 2 or so. The error in the more intense lines is of the order of 50%.

The elementary μ -capture process converts a proton to a neutron, so that, in general, the final nucleus should be Tl with $Z=81$. We expect the γ rays to come from

excited states of Tl^{206} if no neutron is emitted, Tl^{205} if 1 neutron is emitted, Tl^{204} if 2 neutrons are emitted, etc. Our first three γ rays coincide in energy with the transitions from the first excited to the ground state in three of the Tl isotopes. Thus, the reported energy of the $\frac{3}{2}^+ \rightarrow \frac{1}{2}^+$ g.s. in Tl^{205} is 205 keV,^{66,67} for $2^- \rightarrow 0^-$ g.s. in Tl^{206} it is 266.1 keV,⁶⁸ and for $\frac{3}{2}^+ \rightarrow \frac{1}{2}^+$ g.s. in Tl^{203} it is 279 keV.^{66,67} Beyond these, the identification is much less certain. The γ spectra of Tl^{204} and Tl^{206} are known to be very complex,^{68,69} and while several of our energies coincide rather well with those reported, the intensities do not seem to jibe, and we cannot explain why certain intense γ rays that appear in the $\text{Tl}^{203}(n_{\text{th}}, \gamma)\text{Tl}^{204}$ and $\text{Tl}^{205}(n_{\text{th}}, \gamma)\text{Tl}^{206}$ spectra do not appear in our spectrum.

A sizeable fraction (18%) of the μ captures lead to the $\frac{3}{2}^+$ 204-keV first excited state of Tl^{205} , with the emission of 1 neutron. It may be that our 416.1-keV γ is from the $\frac{5}{2}^+ \rightarrow \frac{3}{2}^+$ transition in the same isotope, but our tables^{66,67} give this energy as 410 ± 6 keV, so the identification is somewhat uncertain.

B. Prompt γ Rays

A line appears in both the X and $X\bar{A}$ spectra (Fig. 6) of Pb^{206} at 803 keV. This coincides in energy with the line in the $\Gamma\bar{A}$ spectrum which we already identified as a natural γ ray from the first excited state of Pb^{206} . However, the contribution of this γ ray to the intensity observed in the $X\bar{A}$ spectrum can be estimated from its intensity in the $\Gamma\bar{A}$ spectrum and amounts to only 17%. Thus, the evidence is for a muon-induced *prompt* nuclear γ ray which comes from the first excited state of Pb^{206} .⁷⁰ In Pb^{207} , prompt γ rays at 570 ± 1 and 897 ± 3 keV are found corresponding to the deexcitation of the first and second excited states of this nucleus. Such γ rays would appear to arise from radiationless transitions during the muon cascade which leave the nucleus in an excited state. It is this kind of process which would account for the intensity anomalies which we have discussed above. The intensity found indicates that in this way about 4% of the μ 's leave the nucleus in its first excited state and about 1% in the second excited state. The 803-keV Pb^{206*} γ ray also appears in the Pb^{207} prompt spectrum and both the 570- and 897-keV γ rays

⁶⁶ K. Alder, A. Bohr, J. Huus, B. Mottelson, and A. Winther, *Rev. Mod. Phys.* **28**, 432 (1956).

⁶⁷ B. S. Dželepov, L. K. Peker, and V. O. Sergejev, *Decay Schemes of Radioactive Nuclei* (Academy of Science of USSR Press, Moscow, 1963).

⁶⁸ C. C. Weitkamp, J. A. Harvey, G. G. Slaughter, and E. C. Campbell, *Bull. Am. Phys. Soc.* **12**, 922 (1967); and in *Compendium of Thermal-Neutron Capture γ -ray Measurements*, Parts II and III (to be published); G. A. Bartholomew (private communication).

⁶⁹ W. V. Prestwich, L. B. Hughes, T. J. Kennett, and H. J. Fiedler, *Phys. Rev.* **140B**, 1562 (1965).

⁷⁰ A preliminary report on this work was presented by one of us, C. K. Hargrove, in *Proceedings of the International Conference on Electromagnetic Sizes of Nuclei* (Carleton University, Ottawa, 1967), p. 299.

⁶⁵ T. A. Filippas, P. Palit, R. T. Siegel, and R. E. Welsh, *Phys. Letters* **6**, 118 (1963).

from Pb^{207*} appear in the Pb^{208} prompt spectrum. These could arise if the nuclear excitation induced by the muon in the course of its cascade led to neutron emission. Such radiationless excitation mechanisms have been discussed by Zaretsky and Novikov⁷¹ and by Srinivasan and Sundaresan.⁷² We believe that it is this mechanism that accounts for the muon-induced *prompt* neutron emission which we have observed.⁶⁴ If this interpretation is correct, the deexcitation of the nucleus takes place in the presence of the muon in the $1s$ state. This could cause a shift in energy of the deexcitation γ ray. The shift would imply that the muon sees a different charge distribution for the nucleus in the excited state than in the ground state. Such level shifts have been reported for deformed nuclei.^{73,74}

IX. CONCLUSIONS

We have determined the size and shape of the nuclear charge distribution in Pb from precision measurements of the μ -atomic-transition energies. Since the presence of the muon in the $1s$ orbit produces an appreciable perturbation, which we wanted to measure, we based our determination on the measured energy differences among states with quantum number $n=2$ and 3. The calculated value of the $2p-1s$ transition energy was then found to be 6.8 ± 2.3 keV smaller than the observed value. We attribute this difference to "nuclear polarization," although it includes other effects on the $1s$ level that we have not been able to correct for properly.

We are able to account for all the observed transition energies to better than 1 keV with a simple two-parameter Fermi model for the nuclear charge distribution. This does not fully exploit the precision of our measurements because of uncertainties that remain in the corrections which we do or should apply. A residual perturbation remains in the distribution which we report here. It is principally that caused by the muon in the $2p$ orbit and may amount to 1.7 keV because of nuclear polarization^{31,32} and to 0.7 keV due to higher-order vacuum-polarization effects.¹⁸ Until better means of accounting for such effects are available, it is difficult to see how muonic x rays alone could give any more detail about the nuclear charge distribution, even

in simple spherical nuclei like Pb, than is provided by the Fermi distribution.

The $4f-3d$ and the $5g-4f$ transitions, which even in Pb are quite insensitive to the nuclear parameters in the model used here, provide a check of the vacuum-polarization correction which is just at the limit of the higher-order effects.

The muonic x-ray value of $\langle r^2 \rangle^{1/2}$ is in good agreement with that obtained from the low-energy electron scattering experiments.⁴⁴ Both methods measure this quantity in a fairly model-independent way so that the agreement lends confidence to the validity of the analysis of both measurements. When the higher-energy electron scattering measurements⁴⁵ are analyzed using a Fermi two-parameter model a systematically smaller value of $\langle r^2 \rangle^{1/2}$ results. Since the higher-energy measurements are sensitive to the higher moments of the charge distribution, the lack of agreement implies an inadequacy of the model.⁴⁷ Combining the muonic x ray with the electron scattering measurements offers the best hope for obtaining a more accurate measure of the charge distribution. Once this is done the problem could be turned around and the muonic x rays used to unravel the effects of nuclear polarization and the higher-order radiative corrections.

ACKNOWLEDGMENTS

This experiment would not have been possible except for the generous assistance which we received from many persons. We wish to thank the Atomic Energy Canada, Ltd., Chalk River Nuclear Laboratories for the loan of the Ge detector. In particular, we thank I. L. Fowler and H. L. Malm for their role in fabricating the detector and for their help and advice in mounting it. We are indebted to G. Rogosa of the U.S. Atomic Energy Commission for the loan of isotopically enriched Pb^{207} and Pb^{208} and to D. J. Rokop of the Argonne National Laboratory for the determination of the isotopic composition of our Pb^{206} and natural-Pb targets. M. K. Sundaresan and V. Srinivasan kindly performed the intensity calculation of Table XIX for us. We thank our electronic engineers and technicians J. Lillberg, R. Gabriel, P. Plowe, J. P. Legault, and J. Redfern for the construction and operation of much of the electronic circuitry, especially that having to do with the computer-experiment interface. We were ably assisted in the programming by S. Torres and R. F. Castorf. R. Armstrong prepared the graphs and drawings and our graduate students, H. E. Evans and M. S. Dixit, helped in the running of the experiment. One of us (H.L.A.) wishes to thank Professor G. Wentzel, Professor Y. Nambu, Professor K. W. Ford, and Professor A. Kerman for helpful discussions.

⁷¹ D. F. Zaretsky and V. M. Novikov, Nucl. Phys. **14**, 540 (1959/60); **28**, 177 (1961).

⁷² V. Srinivasan and M. K. Sundaresan, in *Proceedings of the International Conference on Electromagnetic Sizes of Nuclei* (Carleton University, Ottawa, 1967), p. 305.

⁷³ S. Bernow, S. Devons, I. Duerdoth, D. Hitlin, J. W. Kast, E. R. Macagno, J. Rainwater, K. Runge, and C. S. Wu, Phys. Rev. Letters **18**, 787 (1967).

⁷⁴ R. Baader, H. Backe, R. Engfer, K. Hesse, E. Kankeleit, U. Schröder, H. K. Walter, and K. Wien, Phys. Letters **27B**, 425 (1968).